

GEO-FPT: a model of the galaxy bispectrum at mildly non-linear scales

Sergi Novell-Masot,^{a,b} Davide Gualdi,^a Héctor Gil-Marín,^{a,b} Licia Verde^{a,d}

^aICCUB, University of Barcelona, Martí i Franquès, 1, E-08028 Barcelona, Spain

^bInstitut d'Estudis Espacials de Catalunya (IEEC), Barcelona E08034, Spain

^dICREA, Pg. Lluís Companys 23, Barcelona, E-08010, Spain

E-mail: sergi.novell@icc.ub.edu

Abstract. We present GEO-FPT (Geometric Fitted Perturbation Theory), a new model for the galaxy bispectrum anisotropic signal in redshift space, with functional form rooted in perturbation theory. It also models the dependence of the bispectrum with the geometric properties of the triangles in Fourier space, and has a broader regime of validity than state-of-the-art theoretical models based on perturbation theory. We calibrate the free parameters of this model using high-resolution dark matter simulations and perform stringent tests to show that GEO-FPT describes the galaxy bispectrum accurately up to scales of $k \simeq 0.12 h \text{Mpc}^{-1}$ for different cosmological models, as well as for biased tracers of the dark matter field, considering a survey volume of $100 (\text{Gpc } h^{-1})^3$. In particular, a joint analysis of the power spectrum and bispectrum anisotropic signals, taking into account their full covariance matrix, reveals that the relevant physical quantities – the BAO peak position (along and across the line-of-sight), and the growth of structure parameters times the amplitude of dark matter fluctuations, $f\sigma_8$ – are recovered in an unbiased way, with an accuracy better than 0.4% and 2% respectively (which is our 2σ statistical limit of the systematic error estimate). In addition, the bispectrum signal breaks the $f\sigma_8$ degeneracy without detectable bias: f and σ_8 are recovered with better than 2.7% and 3.8% accuracy respectively (which is our 2σ statistical limit of the systematic error estimate).

GEO-FPT boosts the applicability of the bispectrum signal of galaxy surveys beyond the current limitation of $k \lesssim 0.08 h \text{Mpc}^{-1}$ and makes the bispectrum a key statistic to unlock the information content from the mildly non-linear regime in the on-going and forthcoming galaxy redshift surveys.

Contents

| | | |
|----------|--|-----------|
| 1 | Introduction | 1 |
| 2 | Theoretical modelling | 2 |
| 2.1 | Proposed model: Geometric FPT (GEO-FPT) model | 6 |
| 3 | Methodology | 7 |
| 3.1 | Synthetic catalogues | 8 |
| 3.2 | Analysis set-up | 9 |
| 3.3 | Fitting and covariance matrix estimation | 11 |
| 4 | Results | 12 |
| 4.1 | Performance of the model in recovering cosmological parameters | 14 |
| 4.1.1 | QUIJOTE simulations | 15 |
| 4.1.2 | Performance on biased tracers for a WMAP-compatible cosmology | 15 |
| 4.2 | Disentangling the $f\sigma_8$ degeneracy | 18 |
| 4.2.1 | Additional considerations and robustness tests | 19 |
| 4.3 | Testing strong growth factor variations | 20 |
| 5 | Conclusions | 20 |
| A | Covariance matrix estimation and results | 22 |
| B | QUIJOTE complementary results | 24 |
| B.1 | Comparison Quijote-CW simulations | 24 |
| B.2 | Further details on the posterior distributions for QUIJOTE simulations | 26 |
| C | NSERIES complementary results | 28 |

1 Introduction

The power spectrum has long been the primary statistic used for constraining the cosmological parameters and the evolution of perturbations. This is a crucial component for the development of the current cosmological standard model, the Λ CDM model. However, the power spectrum alone would only be sufficient in the case of the description of a purely Gaussian field where, according to Wick’s theorem, all the information of the field is enclosed in the two-point statistics. This is not the case for the galaxy over-density field of the evolved universe, with gravitational collapse (and possibly even primordial fluctuations) being sources of non-Gaussianity.

Hence, higher-order correlations, with the bispectrum as the most straightforward one, can yield further information about the evolution of structure in the universe. Specifically, the bispectrum of large-scale structure surveys can lift degeneracies between cosmological parameters, thus improving the precision in their inference [1–14], especially if the quadrupoles are added [15–19]. Moreover, it is the lowest order correlator which encloses primordial non-Gaussianity information [20–22].

Although the bispectrum has been studied for decades, it has not been applied as widely as the power spectrum to real survey data (see [23–25] as pioneering works on extracting information from the galaxy bispectrum). This is both because of the inherent complexity of the bispectrum formalism, and because of the stringent requirements on control of systematics and on survey size that are needed to confidently measure the bispectrum, and which have only been achieved relatively recently (BOSS and eBOSS [25–28]).

Current and forthcoming surveys (such as DESI¹ [29], Euclid² [30], Vera Rubin³ [31], Roman⁴ [32]) will reach an unprecedented degree of systematics suppression and large survey volumes, making these surveys particularly well-suited to study the bispectrum and other higher-order correlations. It is thus essential to accurately model these summary statistics, in order to obtain reliable results as precisely as possible.

This paper presents a phenomenologically motivated effective bispectrum model in redshift space, the ‘GEO-FPT’ model, that describes the bispectrum monopole and quadrupoles. It consists in a phenomenological modification of the the perturbation theory Z_2 kernel with 5 free parameters, which can vary across redshift. The free parameters are calibrated with bispectrum measurements of the QUIJOTE suite of simulations [33]. This results in a fit which achieves a $\leq 3\%$ accuracy for most of the configurations of the bispectrum monopole, and of $\lesssim 30\%$ for the quadrupoles, for triangles whose sides fulfil $0.02 \leq k \leq 0.12 \text{ h Mpc}^{-1}$ at $z = 0.5, 1, \text{ and } 2$.

This approach differs from other techniques such as [34, 35], where the modifications from SPT come in the form of counterterms that are marginalized over in the cosmological parameter inference. In GEO-FPT, which is similar to the models proposed by [36–38], once the best-fit values for the free parameters are obtained, they remain fixed, assuming that the cosmology dependence of the Z_2 kernel and the form of the kernel’s corrections is weak. This assumption is validated on simulations with different cosmologies.

GEO-FPT’s regime of validity reaches mildly non-linear scales, achieving a significant precision gain with respect to power spectrum-only analyses. We also present a battery of tests which attest that GEO-FPT can be successfully used on the upcoming surveys to exploit the information contained in the bispectrum statistic.

This paper is structured as follows: In Section 2 we provide a brief overview of the perturbation theory models for power spectrum and bispectrum, as well as our new effective model. In Section 3 we present the simulations and the methodology, and in Section 4 we show our main results for the GEO-PT model. In Section 5 we summarize our main findings, and discuss the implications of our work for future surveys and experiments.

2 Theoretical modelling

We start by reviewing the standard perturbation theory formalism for power spectrum and bispectrum in real and redshift space. The shortcomings of this description will motivate the theoretical model we propose.

The real space power spectrum $P_{\delta\delta}$ (which we will use as input for computing the bispectrum) is obtained at 2-loop using the PTCOOL code⁵. In the standard perturbation theory

¹<http://desi.lbl.gov>

²<http://sci.esa.int/euclid/>

³<https://www.lsst.org/>

⁴<https://roman.gsfc.nasa.gov>

⁵<https://github.com/hectorgil/PTcool>

(SPT) framework, it can be expressed at two loops as

$$P_{\delta\delta} = P^L + 2P_{\delta\delta}^{(13)} + P_{\delta\delta}^{(22)} + 2P_{\delta\delta}^{(15)} + 2P_{\delta\delta}^{(24)} + 2P_{\delta\delta}^{(33)}, \quad (2.1)$$

where P^L is the linear power spectrum, obtained with CLASS [39], and the terms $P_{\delta\delta}^{(ij)}$ are loop correction terms, whose explicit expression can be found e.g. in [40] (the dependence on k is implicit). In [41], a modification of the SPT formalism was proposed, denoted renormalized perturbation theory (RPT), which, leaving formally Equation 2.1 unchanged, amends the expressions for $P_{\delta\delta}^{(ij)}$ and improves the accuracy of the SPT power spectrum in the mildly non-linear regime [42]. We will use this approach at two loops (2L-RPT) throughout this work.

The simplest model for bispectrum in real space, that uses perturbation theory at tree level, is referred to as the standard perturbation theory (SPT) model, and can be written as [43]:

$$B(\mathbf{k}_1, \mathbf{k}_2, \mathbf{k}_3) = 2F_2^{\text{SPT}}(\mathbf{k}_1, \mathbf{k}_2)P^L(\mathbf{k}_1)P^L(\mathbf{k}_2) + 2 \text{ perm.}, \quad (2.2)$$

where F_2^{SPT} is the second order (SPT) kernel, given by

$$F_2^{\text{SPT}}(\mathbf{k}_1, \mathbf{k}_2) = \frac{5}{7} + \frac{1}{2} \cos(\theta_{12}) \left(\frac{k_1}{k_2} + \frac{k_2}{k_1} \right) + \frac{2}{7} \cos^2(\theta_{12}), \quad (2.3)$$

where we note as θ_{12} the angle between \mathbf{k}_1 and \mathbf{k}_2 .

The redshift space⁶ galaxy power spectrum, P_g , is calculated from both the non-linear matter power spectrum, $P_{g,\delta\delta}$, the density-velocity, $P_{g,\delta\theta}$, and velocity-velocity, $P_{g,\theta\theta}$, power spectra, according to the TNS model [44, 45],

$$P_g(k, \mu) = D_{\text{FoG}}^P(k, \mu, \sigma_P) [P_{g,\delta\delta}(k) + 2f\mu^2 P_{g,\delta\theta}(k) + f^2\mu^4 P_{\theta\theta} + b_1^2 A^{\text{TNS}}(k, \mu, f/b_1) + b_1^4 B^{\text{TNS}}(k, \mu, f/b_1)], \quad (2.4)$$

where f denotes the logarithmic growth rate of perturbations, and $d \ln \delta / d \ln a$ and $P_{g,\delta\delta}, P_{g,\delta\theta}$ are computed as in [46]. In doing so, we are using the bias expansion $\{b_1, b_2, b_{s2}, b_{3nl}\}$ and assuming the Lagrangian local bias approximation, which has been validated on simulations for haloes [47, 48], as well as BOSS-type galaxies [49]. In Equation 2.4, $A^{\text{TNS}}, B^{\text{TNS}}$ are functions defined in [44], μ is the cosine of the angle of k with the line of sight, and D_{FoG}^P is a damping factor that accounts for the Fingers-of-God (FoG) effect of redshift space distortions [50]. For the power spectrum, we model it as

$$D_{\text{FoG}}^P(k, \mu, \sigma_{\text{FoG}}^P) = \frac{1}{(1 + k^2 \mu^2 \sigma_P^2 / 2)^2}, \quad (2.5)$$

where σ_P is a free parameter to be constrained by the data.

The SPT redshift space bispectrum can then be written in the following way at tree-level order,

$$B^{\text{SPT}}(\mathbf{k}_1, \mathbf{k}_2, \mathbf{k}_3) = D_{\text{FoG}}^B(\mathbf{k}_1, \mathbf{k}_2, \mathbf{k}_3) [2Z_1^{\text{SPT}}(\mathbf{k}_1)Z_1^{\text{SPT}}(\mathbf{k}_2)Z_2^{\text{SPT}}(\mathbf{k}_1, \mathbf{k}_2)P^L(k_1)P^L(k_2) + 2\text{perm.}], \quad (2.6)$$

⁶Here and hereafter we assume flat sky, distant observer approximation.

with the kernels $Z_1^{\text{SPT}}, Z_2^{\text{SPT}}$ being

$$\begin{aligned} Z_1^{\text{SPT}}(\mathbf{k}) &= b_1 + f\mu^2, \\ Z_2^{\text{SPT}}(\mathbf{k}_1, \mathbf{k}_2) &= b_1 F_2^{\text{SPT}}(\mathbf{k}_1, \mathbf{k}_2) + f\mu_{12}^2 G_2^{\text{SPT}}(\mathbf{k}_1, \mathbf{k}_2) + \frac{b_1 f}{2} \left(\mu_1^2 + \mu_2^2 + \mu_1 \mu_2 \left(\frac{k_1}{k_2} + \frac{k_2}{k_1} \right) \right) \\ &\quad + f^2 \mu_1 \mu_2 \left(\mu_1 \mu_2 + \frac{1}{2} \left(\mu_1^2 \frac{k_1}{k_2} + \mu_2^2 \frac{k_2}{k_1} \right) \right) + \frac{1}{2} (b_2 + b_{s^2} S_2^{\text{SPT}}(\mathbf{k}_1, \mathbf{k}_2)), \end{aligned} \quad (2.7)$$

where $\mu_{ij} \equiv (k_i \mu_i + k_j \mu_j) / |\mathbf{k}_i + \mathbf{k}_j|$. The G_2^{SPT} and S_2^{SPT} kernels in SPT are

$$G_2^{\text{SPT}}(\mathbf{k}_1, \mathbf{k}_2) = \frac{3}{7} + \frac{1}{2} \cos(\theta_{12}) \left(\frac{k_1}{k_2} + \frac{k_2}{k_1} \right) + \frac{4}{7} \cos^2(\theta_{12}), \quad (2.8)$$

$$S_2^{\text{SPT}}(\mathbf{k}_1, \mathbf{k}_2) = \cos(\theta_{12})^2 - \frac{1}{3}. \quad (2.9)$$

For the bispectrum, we parametrize the FoG damping factor as [1, 51]

$$D_{\text{FoG}}^B(\mathbf{k}_1, \mathbf{k}_2, \mathbf{k}_3) = (1 + [k_1^2 \mu_1^2 + k_2^2 \mu_2^2 + k_3^2 \mu_3^2]^2 \sigma_B^4 / 2)^{-2}, \quad (2.10)$$

again with σ_B being a free parameter.

In a realistic application, where objects angular positions and redshifts are transformed into co-moving coordinates assuming a fiducial cosmology, the Alcock-Paczynski effect on the survey's summary statistics needs to be accounted for [52].

For the power spectrum and bispectrum this is usually done by introducing the line-of-sight and plane-of-the-sky dilation parameters $\alpha_{\parallel}, \alpha_{\perp}$, which modify k and μ as [46, 53, 54],

$$k \rightarrow \frac{k}{\alpha_{\perp}} \left[1 + \mu^2 \left[\left(\frac{\alpha_{\perp}}{\alpha_{\parallel}} \right)^2 - 1 \right] \right]^{1/2}; \quad \mu \rightarrow \mu \frac{\alpha_{\perp}}{\alpha_{\parallel}} \left[1 + \mu^2 \left[\left(\frac{\alpha_{\perp}}{\alpha_{\parallel}} \right)^2 - 1 \right] \right]^{-1/2}. \quad (2.11)$$

We model the deviations from Poissonian shot-noise with the parameters A_P, A_B , which modify the Poisson prediction as in [38, 54]:

$$P_{\text{noise}} = \left(1 - \frac{A_P}{\alpha_{\parallel} \alpha_{\perp}} \right) P_{\text{Poisson}}, \quad (2.12)$$

$$B_{\text{noise}}(k_1, k_2, k_3) = \left(1 - \frac{A_B}{\alpha_{\parallel}^2 \alpha_{\perp}^4} \right) B_{\text{Poisson}}(k_1, k_2, k_3). \quad (2.13)$$

The power spectrum and bispectrum redshift space multipoles are then obtained by integrating the expansion of the power spectrum and bispectrum dependence on the angle with respect to the line of sight in terms of Legendre polynomials \mathcal{L}_i , so that

$$P^{(\ell)}(k) = \frac{2\ell + 1}{2\alpha_{\parallel} \alpha_{\perp}} \int_{-1}^1 d\mu P(k, \mu) \mathcal{L}_{\ell}(\mu), \quad (2.14)$$

$$B^{(\ell_i)}(\mathbf{k}_1, \mathbf{k}_2, \mathbf{k}_3) = \frac{2\ell + 1}{4\pi \alpha_{\parallel}^2 \alpha_{\perp}^4} \int_{-1}^1 d\mu_1 \int_0^{2\pi} d\phi B(\mathbf{k}_1, \mathbf{k}_2, \mathbf{k}_3) \mathcal{L}_{\ell}(\mu_i), \quad (2.15)$$

Here ϕ is defined as the angle fulfilling $\mu_2 = \mu_1 \cos \theta_{12} - \sqrt{(1 - \mu_1^2)(1 - \cos^2 \theta_{12})} \cos \phi$, and ℓ_i refers to the multipole of order ℓ ($\ell = 0, 2$ corresponding respectively to the monopole

and quadrupole), and the i index denotes which multipole (for instance $\ell = 2$, ℓ_1 being the quadrupole (200)). The power spectrum multipole expansion of 2.14 was proposed in [55, 56], while the bispectrum expansion and choice of variables was first used in [51]. Note that the expansion about the LOS of the bispectrum is not unique; for example in [57] the bispectrum anisotropic signal is expanded in terms of the spherical harmonic decomposition with zero total angular momentum.

The tree-level SPT model for the bispectrum is only valid on large scales, typically for $k \lesssim 0.07 h\text{Mpc}^{-1}$ at $z \sim 0.5$. Note that this k -range is much more restrictive than that routinely used for the power spectrum (with 1-loop or 2-loop SPT modelling) which extends typically to $k \sim 0.15 h\text{Mpc}^{-1}$.

A bispectrum modeling beyond the tree-level formalism is needed to match the k -range of applicability for both power spectrum and bispectrum without introducing unacceptable biases. A valid approach is to perform loop corrections on the bispectrum, see e.g., [58–60].

Alternatively, inspired by previous works [36–38], we propose a phenomenologically motivated bispectrum model, based on tree-level SPT, with few coefficients which we calibrate on simulations, and demonstrate that it is robust against variation in redshift, tracer-type and cosmology.

We build on the findings of [61, 62], where the information content of bispectrum is organized by geometric coordinates of the triangles, and investigate to what extent the bispectrum model can be improved by taking into account these coordinates. To gain physical intuition, Figure 1 illustrates which features of the gravitational bispectrum signal the tree-level SPT model fails to capture. The figure relates the residuals of the tree-level SPT bispectrum normalized by the statistical errorbars of the simulations (normalized residuals), to specific geometric quantities of the triangles. In this figure, and in the rest of the paper, we impose $|\mathbf{k}_1| \leq |\mathbf{k}_2| \leq |\mathbf{k}_3|$, with the specific choices of k -range and Δk being presented in Section 3. In the upper panel of Fig. 1, we display two subsets of triangles, with the ratios $k_2/k_1 = 1.0, 1.8$, which we divide in three bins of area A^7 , represented by the 3 sub-panels, $A < 0.17A_m$, $0.17A_m < A < 0.50A_m$, $A > 0.50A_m$, where A_m denotes the maximum area. In each of these 6 binned subsets of triangles, the normalized residuals are shown as function of the exterior angle θ_{12} between \mathbf{k}_1 and \mathbf{k}_2 . We colour each data-point according to its value of the ratio $\cos(\theta_{\max})/\cos(\theta_{\min})$, where $\theta_{\max}, \theta_{\min}$ are the maximum and minimum (exterior) angles of the triangle. In the lower panel, we show the relationship between the area of triangles and their associated SPT residual.

It is expected that the accuracy of the SPT bispectrum model degrades as k_1 increases. In this set up, for a fixed θ_{12} and a fixed k_1/k_2 ratio, the area is determined by $|k_1|$ and the SPT bispectrum accuracy shows a trend with the area, where larger area triangles are less accurately modeled. There is also a monotonic dependence on θ_{12} . As noted already in the literature [63, 64], for a given k_2 -to- k_1 ratio and a given scale, the accuracy of the SPT bispectrum model depends on the triangle shape i.e., on $\cos \theta_{12}$ (as illustrated by the color scheme).

The dependence on the area is summarized in the bottom panel of Figure 1: there is a clear dependence of the bispectrum residuals with the area of triangles, that becomes more marked with the growth of structure at lower redshifts. Several triangle shapes (several k_1/k_2 ratios and several angles θ_{12}) have a given area, and the residual dependence on these quantities gives rise to a lot of the scatter.

⁷The area of a triangle can easily be computed given the absolute values of k_1, k_2, k_3 by Heron’s formula: $A = \sqrt{s(s - k_1)(s - k_2)(s - k_3)}$, s being the semiperimeter of the triangle, $s = \frac{1}{2}(k_1 + k_2 + k_3)$.

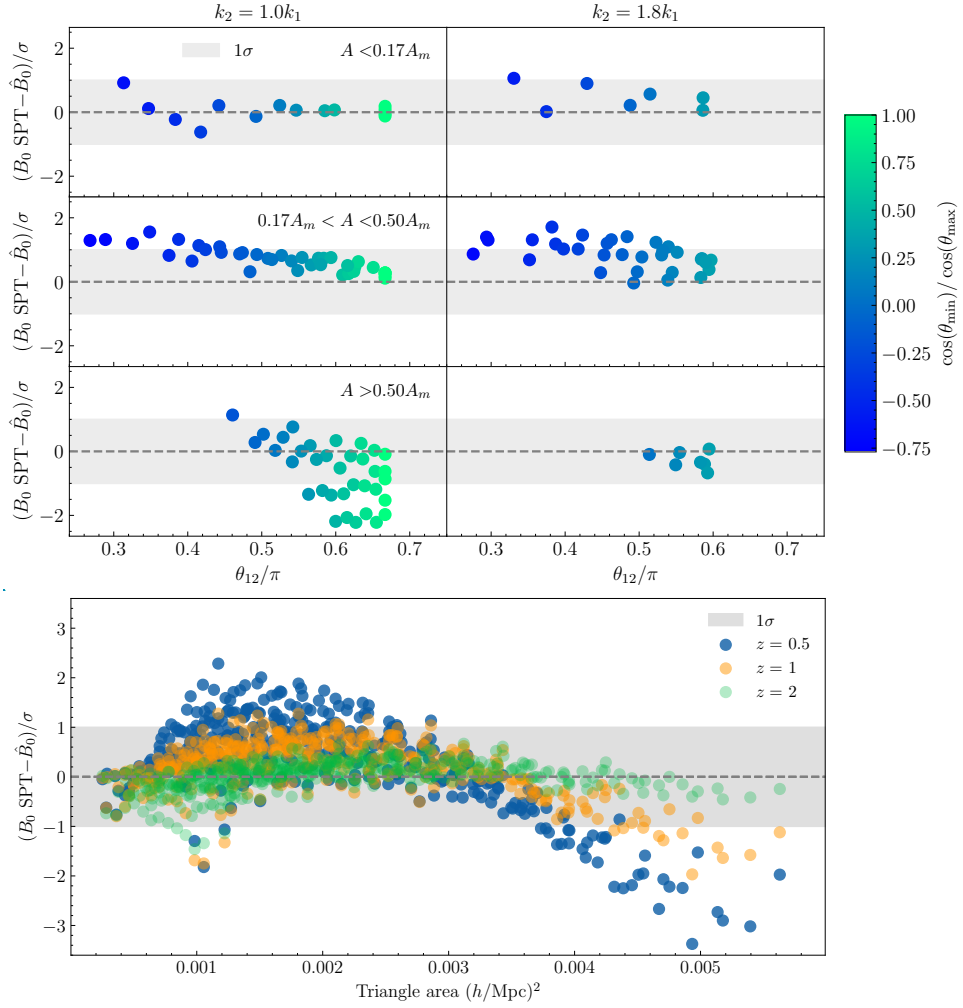


Figure 1. Normalized residuals for the best fit of the SPT redshift-space bispectrum, as a function of the shape and area of the triangles, for $0.02 < k < 0.12$. The only free parameter in the fit is σ_B , governing the incoherent velocity dispersion (FoG) effect. In the panel above we show, for two representative values of k_2/k_1 and for $z = 0.5$, the residuals of the SPT bispectrum as a function of the angle θ_{12} between the vectors \mathbf{k}_1 and \mathbf{k}_2 . The three rows correspond to triangles with different areas, expressed as fraction to the maximum area, A_m . The normalization σ is the expected standard deviation corresponding to a volume of $100 (\text{Gpc } h^{-1})^3$. The colourbar shows the quantity $\cos(\theta_{\max})/\cos(\theta_{\min})$, which is highly sensitive to the shape of the triangle. The lower panel shows the direct dependence between area and accuracy of SPT bispectrum, for $z = 0.5, 1, 2$.

2.1 Proposed model: Geometric FPT (GEO-FPT) model

In what follows we present the Geometric Fitted Perturbation Theory model, which we will refer to as GEO-FPT (GEO in superscripts), that models the dependence of the bispectrum with the geometric properties of the triangles. Motivated by the findings shown in Figure 1, we begin by including the dependence on the triangle area A , by adding two extra terms to the Z_2^{SPT} kernel, respectively proportional to A/A_{norm} and $(A/A_{\text{norm}})^2 - A_{\text{norm}}$ is a constant normalization factor which we define to be $A_{\text{norm}} = 0.001 (h \text{ Mpc}^{-1})^2$. Two additional corrections tackle the dependence on angle. These terms are built from a combination of

ratios of cosines of $\theta_{\max}, \theta_{\text{med}}, \theta_{\min}$ (respectively the maximum, intermediate and minimum external angles of the triangle). The first correction, $\cos(\theta_{\text{med}})/\cos(\theta_{\max})$, quantifies how squeezed the triangle is, while the second ratio, $\cos(\theta_{\min})/\cos(\theta_{\max})$, quantifies how flattened it is⁸. Finally, we add a constant parameter governing the overall amplitude of the bispectrum signal. In summary, we transform $Z_2^{\text{SPT}} \rightarrow Z_2^{\text{GEO}}$, as follows

$$Z_2^{\text{GEO}} = Z_2^{\text{SPT}} \times \left[f_1 + f_2 \frac{\cos(\theta_{\text{med}})}{\cos(\theta_{\max})} + f_3 \frac{\cos(\theta_{\min})}{\cos(\theta_{\max})} + f_4 \frac{A}{A_{\text{norm}}} + f_5 \frac{A^2}{A_{\text{norm}}^2} \right]. \quad (2.16)$$

where the coefficients f_1, \dots, f_5 should be calibrated on N-body simulations and mock galaxy surveys. In this model, the F_2 and G_2 kernels maintain the same expressions as in SPT and the correction is the same for all redshift space multipoles. Besides the Z_2 kernel, the other change of the GEO-FPT model, compared to Equations 2.2 and 2.6, is that the input power spectrum is not the linear one P^L but rather the non-linear power spectrum $P_{\delta\delta}$ from Equation 2.1. In Appendix C we explore whether having different best-fit parameters f_1, \dots, f_5 for the monopole and quadrupoles can yield an improvement in accuracy and precision, finding no substantial gain in doing so.

The FoG parameters σ_P, σ_B are always treated as nuisance parameters and marginalized over. The shot-noise parameters A_P, A_B are kept fixed at their fiducial values of unity when fitting the $\{f_1, \dots, f_5\}$ kernel coefficients, then they are used as nuisance parameters in parameter inference and thus marginalized over.

In summary, the complete form of the GEO-FPT bispectrum reads as

$$B^{\text{GEO}}(\mathbf{k}_1, \mathbf{k}_2) = D_{\text{FoG}}^B(\mathbf{k}_1, \mathbf{k}_2) \left[2Z_1^{\text{SPT}}(\mathbf{k}_1)Z_1^{\text{SPT}}(\mathbf{k}_2)Z_2^{\text{GEO}}(\mathbf{k}_1, \mathbf{k}_2)P^{\text{NL}}(k_1)P^{\text{NL}}(k_2) + 2\text{perm.} \right], \quad (2.17)$$

where P^{NL} indicates the real space non-linear power spectrum, and $\mathbf{k}_3 = -\mathbf{k}_1 - \mathbf{k}_2$ is implicit. In this paper P^{NL} is given by Equation 2.1 and computed at 2L-RPT with PTcool⁹ and BRASS¹⁰, but other models (such as HALOFIT [65, 66]) could be used.

3 Methodology

We fit the 5 free parameters of the Z_2^{GEO} Eq. 2.16 to measurements of bispectrum from a large sample of dark matter N-body simulations provided by the QUIJOTE suite [33] (8000 independent realizations at $z = 0.5$ and 4000 realizations at $z = 1, 2$), where the measurements are carried out using the pipeline of [22, 67]. When calibrating the f_1, \dots, f_5 parameters with the QUIJOTE simulations, the cosmological parameters $\sigma_8, f, \alpha_{\parallel}, \alpha_{\perp}$ are kept fixed at the respective true values, together with the bias parameters b_1, b_2 and the shot-noise parameters A_P, A_B . Then the parameters $f_1, \dots, f_5, \sigma_B$ are left free to vary, with effectively improper uniform priors¹¹. On the other hand, when using the bispectrum model to recover the cosmology (from Section 4.1.1), the f_1, \dots, f_5 kernel parameters are kept fixed at the best-fit value. All other parameters have again broad uniform priors, with the exception of A_P, A_B , for which we

⁸For triangles satisfying $k_1 \leq k_2 \leq k_3$, a triangle will be considered to be squeezed if $k_3 \sim k_2 \gg k_1$, and flattened if $k_1 \sim k_2 \gtrsim k_3/2$.

⁹<https://github.com/hectorgil/PTcool>

¹⁰<https://github.com/hectorgil/Brass>

¹¹The priors are sufficiently broad that the MCMC never samples the prior boundary.

use Gaussian priors¹² with mean 1 and *rms* 0.5. This prior becomes unimportant when the shot noise matters (i.e., in the NSERIES simulations). We also employ other sets of simulations to assess the performance of the GEO-FPT bispectrum model for different cosmologies and for computing the necessary covariance matrices as we describe in the following section.

3.1 Synthetic catalogues

We use four independent sets of simulations, summarized in Table 1. The baseline results are presented for the QUIJOTE simulations, which feature 512^3 dark matter (DM) particles, evolving gravitationally in a periodic box of side $L_{\text{box}} = 1 \text{ Gpc } h^{-1}$, where initial conditions are set by 2LPT (second-order Lagrangian perturbation theory [68–70]). We re-use the 8000 power spectrum and bispectrum measurements performed in the previous work [67], and we further estimate the bispectrum on 4000 realizations for $z = 1, 2$. In order to determine the covariance of these measurements, we use the same 4000 (8000) realizations and re-scale the covariance so it corresponds to that of a large-enough volume¹³ of $100 (\text{Gpc } h^{-1})^3$. Since the data-vector has of the order of ~ 1200 elements per redshift bin, this choice of 4000 realizations strikes a good compromise between computational time and accuracy of signal and covariance matrix. The cumulative volume of the 4000 (8000) simulations is enough to make the statistical errors in the measured bispectrum signal completely negligible compared to the size of the errors given by the covariance we apply: the fitting residuals are entirely due to modeling systematics.

| Name (type) | Ω_m | Ω_b | σ_8 | n_s | f | h | N_{sims} | L_{box} |
|----------------|------------|------------|------------|--------|-------|--------|-------------------|------------------|
| QUIJOTE (DM) | 0.3175 | 0.049 | 0.834 | 0.9624 | 0.534 | 0.6711 | 8000; 4000 | 1 |
| NSERIES (Gal.) | 0.286 | 0.047 | 0.82 | 0.96 | 0.504 | 0.6711 | 7 | 2.6 |
| PATCHY (Gal.) | 0.307 | 0.048 | 0.829 | 0.961 | 0.525 | 0.678 | 2000 | 2.5 |
| CW-Fid (DM) | 0.27 | 0.047 | 0.79 | 0.95 | 0.483 | 0.7 | 160 | 2.4 |
| CW-0.2 (DM) | 0.2 | 0.035 | 0.872 | 0.95 | 0.413 | 0.8133 | 1 | 2.79 |
| CW-0.4 (DM) | 0.4 | 0.07 | 0.693 | 0.95 | 0.604 | 0.5751 | 1 | 1.97 |
| CW-1 (DM) | 1 | 0.173 | 0.493 | 0.95 | 1 | 0.3637 | 1 | 1.25 |

Table 1. Main cosmological parameters for all sets of simulations considered in this work. The QUIJOTE simulations (the dark matter particles distribution) are used for calibrating the model at $z = 0.5, 1.0, 2.0$, as well as a first consistency check. The NSERIES measurements (galaxy mocks, where galaxies are painted on top of N-body halos) are used for checking that the model recovers the underlying cosmological parameters in a different cosmology and that it works with biased tracers. The PATCHY mocks consist of a large set of 2000 realizations of fast-mocks (not N-body) which mimic the 2- and 3-point statistics observed by BOSS. The CW-Fid, 0.2, 0.4, 1 simulations (dark matter particles distribution) allow an assessment of the validity of the model as Ω_m is varied, while leaving $\Omega_m h^2$ unchanged. L_{box} is expressed in units of $[\text{Gpc } h^{-1}]$.

The underlying cosmology of this simulations set is characterized by the following cosmological parameters: the matter and baryon densities, $\Omega_m = 0.3175, \Omega_b = 0.049$, the amplitude of dark matter fluctuations, $\sigma_8 = 0.834$, the scalar spectral index, $n_s = 0.9624$, the reduced Hubble constant, $h = 0.6711$, and the neutrino mass $M_\nu = 0$; which are fully compatible with Planck best-fit results [71].

¹²This prior is physically-motivated: in the QUIJOTE simulations the shot noise is negligible.

¹³Since our adopted data vector, as explained in Section 3.2, is the mean of the statistics from the 8000 (4000) realizations, it effectively corresponds to the signal of a volume of 8000 (4000) $(\text{Gpc } h^{-1})^3$.

To assess how the model captures the cosmology and galaxy-bias model dependencies, we employ the NSERIES periodic box mocks¹⁴ [72–74]. This is a set of 7 independent realizations of dark matter simulations at $z = 0.5$, where haloes are populated with galaxies according to a Halo Occupation Distribution compatible with BOSS clustering data, where the average density of galaxies is $\bar{n} \simeq 4 \times 10^{-4}$. The cosmological parameters are consistent with WMAP9 best-fit cosmology [75]: $\Omega_m = 0.286$, $\Omega_b = 0.047$, $\sigma_8 = 0.82$, $n_s = 0.96$, $h = 0.7$. Each realization consists of a cubic box whose side is $L_{\text{box}} = 2.6 \text{ Gpc } h^{-1}$. The total physical volume for the 7 boxes is $123 (\text{Gpc } h^{-1})^3$, corresponding to an effective volume of $80 (\text{Gpc } h^{-1})^3$, with the effective volume computed from the physical volume following [76]. The full data-vector for the NSERIES analysis has 441 elements; since 7 realizations are not enough for estimating the covariance of this data-vector, we employ instead the 2000 realizations of the cubic PATCHY galaxy fast-mocks [77] with $z = 0.53$ and $L_{\text{box}} = 2.5 \text{ Gpc } h^{-1}$, which were also produced for their application to the BOSS analysis. Each of these mocks has on average $\sim 185^3$ galaxies, resulting in $\bar{n} \simeq 4 \cdot 10^{-4}$, and therefore very close to the signal-to-noise ratio of NSERIES. In this case, the cosmological parameters are $\Omega_m = 0.307$, $\Omega_b = 0.048$, $\sigma_8 = 0.829$, $n_s = 0.961$, $h = 0.678$. We average the covariance of these realizations to match the physical volume of the mean of the 7 NSERIES simulations.

The behaviour and validity of our model is also tested on a wider range of cosmological parameters by including the set of dark matter simulations that was used in previous bispectrum works [37, 38] and presented in [78], which we refer to as ‘CW’. The CW simulations consist of a set of 160 realizations of 768^3 DM particles, with a cosmology consistent with WMAP9 (see summary Table 1), together with one realization at each of the three following values of $\Omega_m = 0.2, 0.4, 1.0$, keeping $\Omega_m h^2$ and the primordial amplitude of scalar fluctuations, A_s , fixed in real space. These three additional simulations have the same initial conditions as the *first-index* realization of the fiducial set (with $\Omega_m = 0.27$), and therefore their fluctuations due to cosmic variance are very similar, allowing us to compute cosmology variations by only looking at the relative variations across these four cosmologies. All CW periodic boxes have the same size in units of Gpc, $L_{\text{box}} = 3.43 \text{ Gpc}$, and their size in units of $\text{Gpc } h^{-1}$ varies according to the value of h in each, being $L_{\text{box}} = 2.4 \text{ Gpc } h^{-1}$ for the fiducial WMAP9 cosmology. The estimation of their covariance matrix, starting from the QUIJOTE simulations set, is described in Appendix A.

All the simulations are flat- Λ CDM, with dark energy equation of state parameter $w = -1$, and their specs are summarized in Table 1.

3.2 Analysis set-up

We consider our “data vectors” as the summary statistic’s averages of *all* the available realizations (the simulation boxes). As such, the statistical error of these data vectors is the one corresponding to the total cumulative simulations volumes (Section 3.1) hence negligible, especially for the QUIJOTE simulations.

The redshift space power spectrum data-vector consists of the power spectrum monopole and quadrupole, $\{P_0, P_2\}$, from $k_{\text{min}} = 0.02 \text{ Mpc } h^{-1}$ up to a certain k_{max} . For simplicity, we will refer to this power spectrum data-vector simply as the power spectrum, or P_{02} . The bispectrum data-vector consists of the three following multipoles, the monopole and the k_1 - and k_2 -quadrupoles, $\{B_0, B_{200}, B_{020}\}$, respectively. We will refer to this data-vector just as bispectrum, B_0, B_{02} , depending on whether we want to consider the isotropic component

¹⁴<https://www.ub.edu/bispectrum/page12.html>

only, or the full anisotropic component. Note that for the B_{200} and B_{020} quadrupoles the configurations fulfilling $k_1 = k_2$ are equal, so they can't be considered in both quadrupoles –otherwise the covariance matrix would be singular. We opt for just accounting them on B_{200} . Therefore, the number of elements on B_{200} is slightly larger than on B_{020} . The data vectors are measured using the methodology and pipeline presented in [22, 67].

We have found that using the three k_1 -, k_2 - k_3 -based quadrupoles, $\{B_0, B_{200}, B_{020}, B_{002}\}$ does not significantly improve the cosmology constraints compared to our baseline data-vector choice $\{B_0, B_{200}, B_{020}\}$, as also reported by [79]. Hence, for simplicity we will not consider the B_{002} quadruple in the analysis of this paper.

We use a modified version of RUSTICO¹⁵ to compute the bispectrum from the simulations, and the GEO-FPT bispectrum code.¹⁶

For our baseline analysis, we consider a k -range for the power spectrum of $0.02 < k[h \text{ Mpc}^{-1}] < 0.15$ (unless otherwise stated, in some cases we use a $k_{\text{max}}^P = 0.12 [h \text{ Mpc}^{-1}]$), while for the bispectrum we focus on the range $0.02 < k[h \text{ Mpc}^{-1}] < 0.12$, both when fitting for the f_1, \dots, f_5 model parameters, and when inferring the cosmological parameters. This k -range is chosen as to capture the statistics in the linear and mildly non-linear regime. Furthermore, we find this set-up to be sufficient for representing most triangle configurations of interest, including squeezed triangles up to $k_3 \sim k_2 \sim 5k_1$.

Special attention must be given to the power spectrum and bispectrum k -bins, Δk . Our choice of Δk results from a trade off between two competing effects. To minimize binning effects, Δk should be as close as possible to k_f . However, a small bin size yields a large number of triangles, which are highly correlated and for which the covariance matrix should be estimated from simulations. Given the available number of simulations (8000 (4000) realizations for the QUIJOTE simulations), we choose $\Delta k = 1.1k_f^Q \approx 0.0069 h \text{ Mpc}^{-1}$ for all the analyses involving the QUIJOTE simulations (Sections 4, 4.1.1). Also, as commented in Appendix A, we use the QUIJOTE covariance for the analysis of the CW simulations in Section 4.3, so we choose $\Delta k = 1.1k_f^Q$ again for this case. For the NSERIES analysis, we opt for $\Delta k = 0.01 h \text{ Mpc}^{-1}$, motivated by the available number of mocks, 2000.

As pointed out in [80–82], there is a so-called binning effect that, if not accounted for, can introduce systematic errors. The wider the bin, with respect to the fundamental frequency $k_f = 2\pi/L_{\text{box}}$, the bigger the binning effect. In fact, the elements of the data vector are binned measurements: the measured power spectra (resp. bispectra) is an average of all k -vectors (triangles) that are contained in the k -bin. The theoretical model on the other hand is usually computed at a single representative k per bin. This “effective” k is computed for the power spectrum as

$$k^{\text{eff}} = \frac{1}{N(k)} \sum_{\mathbf{q}_i \in k_1} q_i, \quad (3.1)$$

with $N(k)$ the number of configurations in the bin. For the bispectrum, it translates as

$$k_i^{\text{eff}}(k_1, k_2, k_3) = \frac{1}{N(k_1, k_2, k_3)} \sum_{\mathbf{q}_1 \in k_1} \sum_{\mathbf{q}_2 \in k_2} \sum_{\mathbf{q}_3 \in k_3} q_i \delta_K(\mathbf{q}_1 + \mathbf{q}_2 + \mathbf{q}_3), \quad (3.2)$$

where $i = 1, 2, 3$, and again $N(k_1, k_2, k_3)$ is the number of configurations in the bin. As stated above, to minimize the binning effect we consider a bin size of $\Delta k = 1.1k_f$.

¹⁵<https://github.com/hectorgil/Rustico>

¹⁶<https://github.com/serginovell/Geo-FPT>

For the power spectrum this procedure still leaves some residual effect due to incomplete mode-sampling for the wider bins at low $|\mathbf{k}|$. We correct for this as in [82] by introducing G , the binning factor, defined as the ratio between the average of the fiducial model power spectrum of all the k in a given bin and the fiducial model power spectrum evaluated at the effective k for that k -bin,

$$G(k_j^{\text{eff}}) \equiv \frac{\langle P^{\text{model}}(k \in \text{bin } j) \rangle}{P^{\text{model}}(k_j^{\text{ef}})}, \quad (3.3)$$

in order to correct the power spectrum measurements as $P^{\text{meas}} \rightarrow G^{-1} P^{\text{meas}}$. We have further checked for the effect of the uneven distribution of μ across all k -vectors in a bin, but found its magnitude to be negligible.

In the bispectrum this effect is, in principle, even more important, since the condition of triangle closure causes each bin to have proportionally less configurations per data vector element than in the power spectrum. Nevertheless, the nature of our proposed effective formula, the procedure for fitting its coefficients, together with having a small Δk and working with k^{eff} defined as in Equation 3.2, accounts for most of the effect. Still, flattened triangles, which are most affected by the binning effect [60], are omitted in our analysis by imposing the condition $k_3 - (k_2 + k_1) > \Delta k$. (recall that $k_1 \leq k_2 \leq k_3$).

3.3 Fitting and covariance matrix estimation

The procedure we choose to fit the free parameters of the kernels to the measurements and then to perform parameter inference with our calibrated GEO-FPT bispectrum model, is a Markov chain Monte Carlo sampling, MCMC, specifically using the EMCEE algorithm [83]. In the MCMC sampling, we specify broad, uniform priors¹⁷ in the parameters, and calculate the logarithm of the likelihood assuming Gaussianity and applying the Sellentin-Heavens correction [84], as

$$\log L \propto -\frac{n}{2} \ln \left(1 + \frac{(\mathbf{D}_{\text{meas.}} - \mathbf{D}_{\text{th.}}) \text{Cov}_{\mathbf{D}_{\text{meas.}}}^{-1} (\mathbf{D}_{\text{meas.}} - \mathbf{D}_{\text{th.}})^T}{n - 1} \right), \quad (3.4)$$

where n is the number of simulations and \mathbf{D} denotes the data vector. For fitting the GEO-FPT bispectrum coefficients f_1, \dots, f_5 , the data vector is $\mathbf{D} = \{B_0, B_{200}, B_{020}\}$, while for parameter inference the data vector is the full set $\{P_0, P_2, B_0, B_{200}, B_{020}\}$. The covariance matrix for the bispectrum-only data vector is a subset of the full $P_{02} + B_{02}$ covariance.

The full covariance matrix for the data vector is thus an essential component of the analysis. The covariance between different bispectra configurations, and the covariance between power spectrum and bispectrum should not be ignored [7, 85–87]. Thus, an analytical computation of the covariance matrix is highly non-trivial: if possible, the covariance matrix $\text{Cov}_{\mathbf{D}_{\text{meas.}}}$ should be estimated from simulations. If the required simulations are not available, it is possible to resort to hybrid approaches where the covariance model is calibrated on mocks [16, 22, 88]. A detailed account of our covariance matrix estimation can be found in Appendix A.

Each covariance matrix is estimated from the simulations measurements at each redshift; it is then rescaled to obtain errorbars matching the target volume, with specific rescaling factors in Appendix A. In summary, to fit the f_1, \dots, f_5 coefficients we use a covariance matrix

¹⁷Effectively these are uniform improper priors because the MCMC never samples the prior boundary.

corresponding to the total volume of the simulations (that is the actual statistical error associated with the mean data vector). To do cosmological inference, when needed, we rescale the covariance matrix to correspond to a survey volume of $\sim 100(\text{Gpc } h^{-1})^3$.

The reduced covariance matrix, $R_{\text{cov}}^{ij} = \text{Cov}^{ij} / \sqrt{\text{Cov}^{ii} \text{Cov}^{jj}}$, for the bispectrum-only data vector is shown in Figure 2, together with the resulting best fit bispectrum for each multipole and redshift. The power spectrum-bispectrum cross-covariance is reported in Appendix A.

The best-fit f_1, \dots, f_5 coefficients and their errorbars for each redshift snapshot can be found in Table 2, while the corresponding posterior distributions are shown in Appendix B, in Figure 11.

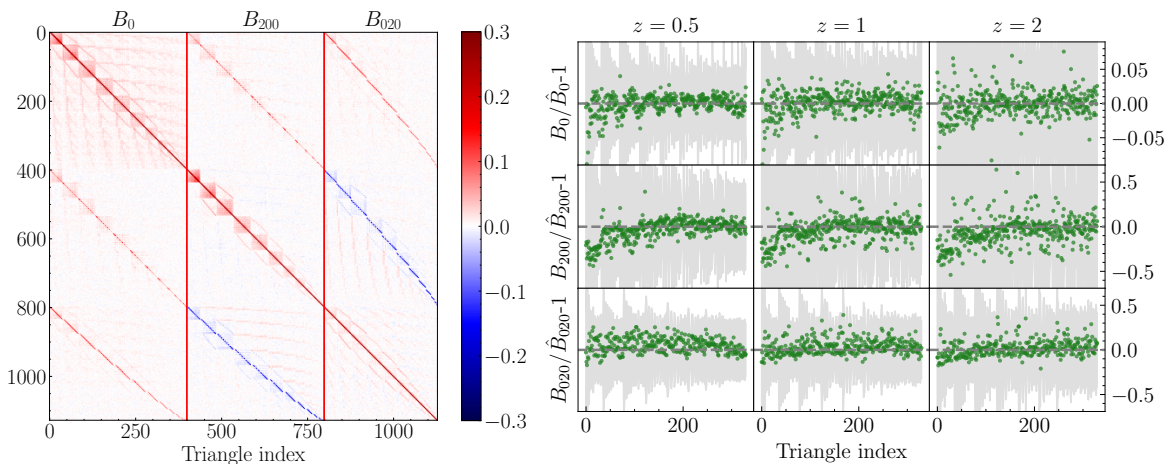


Figure 2. Left panel: reduced covariance matrix of the data-vector formed by $\{B_0, B_{200}, B_{020}\}$, obtained with the QUIJOTE simulations at $z = 0.5$. The red vertical lines together with the titles in the top x axis indicate how the data vector elements are mapped to the summary statistics. We can observe how, aside from the correlation between the same triangle configuration for different multipoles, there is structure in the covariance matrix, indicating correlation between different configurations. Right panel: ratio between the best fit and the QUIJOTE measurements, for all triangle configurations and all the considered multipoles at each of the snapshots at $z = 0.5, 1, 2$. The cosmology is kept at the fiducial values, and the k -range is the same as for the fit, $0.02 < k[h \text{ Mpc}^{-1}] < 0.12$. The dashed grey area represents the variance of the measurements, for a volume of $100 (\text{Gpc } h^{-1})^3$.

In practice, we advocate using the estimated best fit values for the GEO-FPT correction coefficients and interpolating the values of $\{f_1, f_2, f_3, f_4, f_5\}$ for intermediate redshifts via spline or linear interpolation, as implemented in [our code](#).

4 Results

After the fitting of the coefficients of the Z_2^{GEO} kernel, we obtain a bispectrum theory model whose discrepancy with the measurements from simulations at $z = 0.5, 1, 2$ mostly does not surpass 3% in the case of B_0 , and 30% in the case of B_{200} and B_{020} , as seen in Figure 2. This is well within the statistical error for a volume of $\lesssim 100 (\text{Gpc } h^{-1})^3$. Additionally, we compare the GEO-FPT fit for the monopole at $z = 0.5$ against the prescription from SPT in Figure 10 of Appendix B.

In Figure 3 we show the dependence of the best-fit coefficients on redshift, where the errorbars correspond to the total size of the simulations, 8000 and 4000 $(\text{Gpc } h^{-1})^3$ for $z = 0.5$

and $z = 1, 2$ respectively. The shaded region represents the statistical error for a volume of $100 (\text{Gpc } h^{-1})^3$. The dependence with redshift is very mild, which already suggests that the Z_2^{GEO} formula is expected to be stable upon changes of the cosmology. We will further show this in Sections 4.1.2 and 4.3.

| Parameter ($\pm 1\sigma$) | $z = 0.5$ | $z = 1$ | $z = 2$ |
|-----------------------------|-----------------------|-----------------------|---------------------|
| f_1 | 1.0033 ± 0.0024 | 1.0180 ± 0.0038 | 1.037 ± 0.0049 |
| f_2 | -0.0040 ± 0.0018 | -0.0041 ± 0.0031 | 0.0020 ± 0.0041 |
| f_3 | 0.0240 ± 0.0014 | 0.0149 ± 0.0024 | 0.0056 ± 0.0033 |
| f_4 | -0.0568 ± 0.0015 | -0.0547 ± 0.0024 | -0.048 ± 0.0033 |
| f_5 | 0.01325 ± 0.00029 | 0.01144 ± 0.00046 | 0.0081 ± 0.0006 |

Table 2. Best-fit parameters $\{f_1, \dots, f_5\}$ for the Z_2^{GEO} kernel, for the redshifts $z = 0.5, 1, 2$. The fits were performed following the set-up described in 3, using $n_{\text{sim}} = 8000-4000$ QUIJOTE simulations respectively for $z = 0.5$ and $z = 1, 2$, for both estimating the signal and the covariance matrix. The covariance matrix is rescaled so that the errorbars correspond to the total volume of the sample, which is equal to $n_{\text{sim}} \times 1(\text{Gpc } h^{-1})^3$.

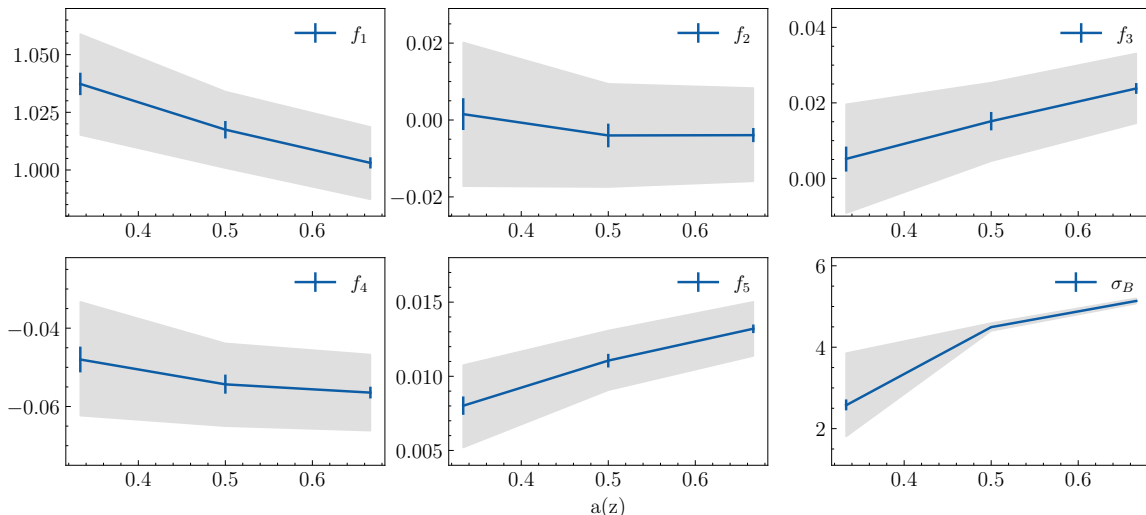


Figure 3. Dependence on redshift for the kernel coefficients $\{f_1, f_2, f_3, f_4, f_5\}$ and the FoG parameter σ_B : quantities are shown as a function of $a(z) = 1/(1+z)$ for $z = 0.5, 1, 2$. The best fits have been obtained using the fiducial set of QUIJOTE for both the signal and covariance matrix estimation. We assume no cross-covariance across different redshifts, and at each redshift the covariance used corresponds to the volume of the total number of simulations. The shaded region shows the resulting 1σ statistical uncertainty for a volume of $100 (\text{Gpc } h^{-1})^3$. The coefficients are obtained from a fit to the data-vector $B_0 + B_{200} + B_{020}$, with a constant k -range across redshift and multipoles of $0.02 < k(h \text{ Mpc}^{-1}) < 0.12$.

Additionally, in Figure 4 we visualize the effect on the GEO-FPT bispectrum monopole model of each individual kernel coefficients, at $z = 0.5$. In each panel one coefficient is displaced from the best fit by plus/minus one standard deviation, while all other coefficients are kept fixed at their best-fit value. The bottom-right panel helps with the interpretation of the triangle index in term of triangles shape.

As expected, f_1 , which acts as an amplitude parameter, uniformly displaces the model across all configurations. The effect of the f_2 parameter can be understood as follows: f_2 modulates the term $\cos \theta_{\text{med}} / \cos \theta_{\text{max}}$, which goes to zero for the very squeezed triangles and is 1 for the equilateral and flattened triangles. Hence f_2 leaves unchanged a small number of configurations, while acting very similarly to f_1 for all others. The f_3 term on the other hand changes sign between flattened and equilateral configurations; because of this, f_3 has a very low correlation with the other parameters (see Figure 11). The f_4 and f_5 parameters, which modulate the terms proportional to A and A^2 respectively, obviously become relevant at triangles with large area. We can see the two parameters are complementary since changes of f_5 target more strongly the non-linear configurations, while f_4 affects triangles from the linear regime as well.

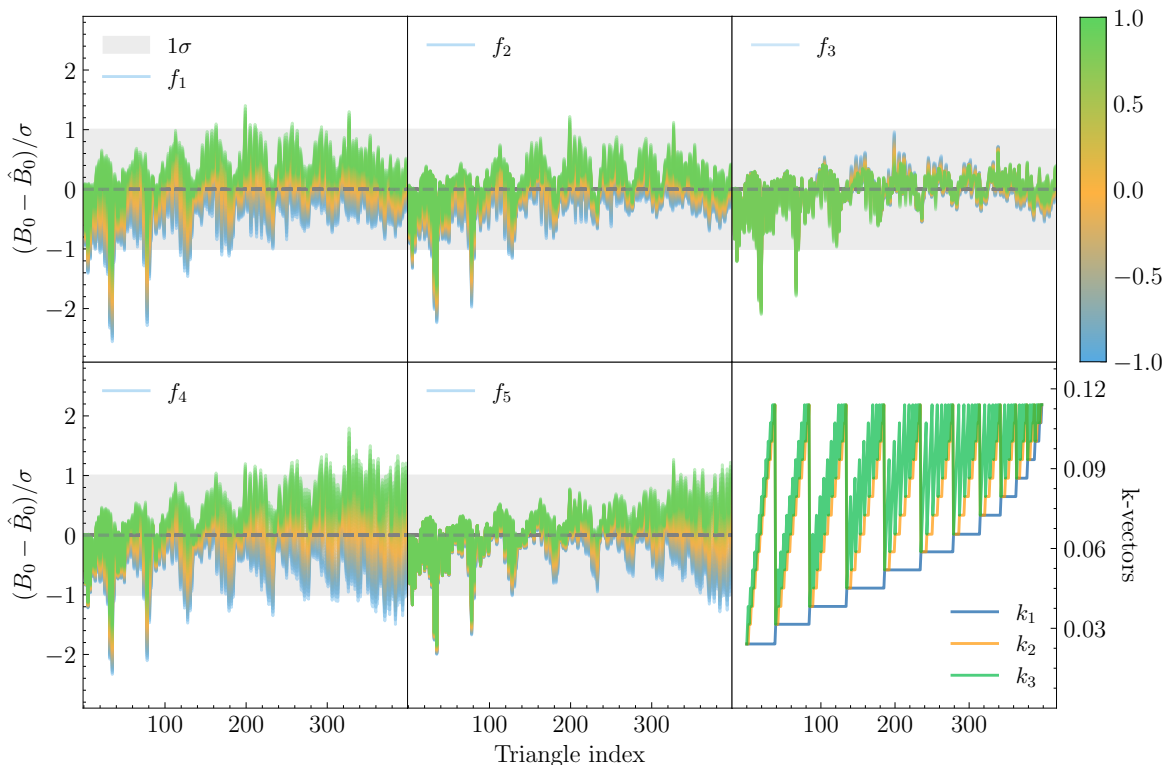


Figure 4. We show how (conditional) variations of 1σ (described by the colourbar) for each parameter of the Z_2^{GEO} kernel affect the fit of the bispectrum monopole B_0 to the mean of the simulations measurements. The bottom right plot shows the correspondence between the configurations and the values of k_1, k_2, k_3 of the triangle.

4.1 Performance of the model in recovering cosmological parameters

We next quantify how well our QUIJOTE-calibrated GEO-FPT model can recover the original parameters of the simulations when used for cosmological inference. Since the statistical errors involved in the fit of the kernel’s coefficients are negligible compared to the systematic errors, this procedure tests if the adopted GEO-FPT model is significantly biased.

We test the model first with the QUIJOTE suite of simulations in Section 4.1.1, to then assess the performance of the model in the case of biased tracers and different cosmology, in

Section 4.1.2. In these first two subsections, we focus on the set of parameters $\{f\sigma_8, \alpha_{\parallel}, \alpha_{\perp}\}$. In Section 4.2 we focus on the bispectrum role in breaking the $f\sigma_8$ degeneracy that is naturally present in the power spectrum. Finally, we will provide a further test on unbiased tracers but a cosmology with very different matter density parameter (Section 4.3, CW simulations).

4.1.1 QUIJOTE simulations

We perform an MCMC sampling of the parameter space $\{b_1\sigma_8, b_2\sigma_8, f\sigma_8, \alpha_{\parallel}, \alpha_{\perp}, A_P, A_B, \sigma_P, \sigma_B\}$, using the effective Z_2^{GEO} kernel with its coefficients fixed at the best fit values (reported in Table 2). We refer to this as the (QUIJOTE)-calibrated Z_2^{GEO} kernel. All priors are effectively improper uniform except for A_P and A_B , where we impose a normal distribution $\mathcal{N}(1, 0.5)$ as recommended in [89]. In Figure 5 we show the 1 and 2D posterior distributions for the cosmological parameters of interest for the data-vectors $P_{02} + B_0$ and $P_{02} + B_{02}$ at $z = 0.5$; $A_P, A_B, \sigma_P, \sigma_B$ are considered nuisance parameters and are marginalized over. The errorbars correspond to a volume of $100 (\text{Gpc } h^{-1})^3$, which is suitable to assess whether possible systematic biases in the recovered parameters are significant compared to the statistical errors expected from future surveys. The central values and 1σ errors for the cosmological parameters are reported in Table 3. Results for the $P_{02} + B_{02}$ data-vectors at $z = 1, 2$ can be found in Appendix B. In all cases the Z_2^{GEO} kernel is calibrated to the full data-vector $B_0 + B_{200} + B_{020}$.

For all data-vectors considered, all parameters are recovered within 1σ (the fiducial values at this redshift are $f\sigma_8 = 0.489$, while of course $b_1 = 1, b_2 = 0, \alpha_{\parallel} = \alpha_{\perp} = 1$). The $P_{02} + B_{02}$ data-vector notably reduces the errorbars compared to those obtained with $P_{02} + B_0$ (or P_{02} alone), by factors of 63 and 31% for α_{\parallel} and α_{\perp} respectively (see Table 3).

In the next subsection we test the performance of the GEO-FPT bispectrum model on biased tracers and a slightly different cosmology (Section 4.1.2, NSERIES mocks). In Section 4.2 we will explore the improvement that the anisotropic bispectrum provides to the inference of the parameters f and σ_8 separately.

4.1.2 Performance on biased tracers for a WMAP-compatible cosmology

We now turn to the NSERIES galaxy simulations. These simulations, described in Section 3.1, differ from QUIJOTE in the fiducial cosmological parameters and, most importantly, allow us to test the performance of the model in describing the galaxy bispectra, when extended to include the bias expansion of Eq. 2.7. The coefficients of the Z_2^{GEO} kernel remain fixed to the values obtained in the fit with QUIJOTE.

We perform the MCMC to explore the cosmological parameter space posteriors for the same parameters and priors as for QUIJOTE, (in this case the prior on A_P and A_B is not important, given that the shot noise signal is larger) using the NSERIES data vectors and the covariance obtained from the PATCHY mocks. The main results are presented in Figure 6 and Table 3. In this case, the fiducial quantities for the clustering parameters are $\sigma_8 = 0.637, f = 0.737$, resulting in $f\sigma_8 = 0.469$. The bias parameters b_1, b_2 have no value known *a priori*, so they are marginalized over, together with the $\sigma_P, \sigma_B, A_P, A_B$ parameters, as before.

We show the posterior distributions for $P_{02} + B_0$ and $P_{02} + B_{02}$, together with the constraints obtained from the P_{02} data-vector, for comparison. In the set of parameters $\{f\sigma_8, \alpha_{\parallel}, \alpha_{\perp}\}$, the addition of B_0 tightens the constraints by a factor of $\sim 10\%$. This is expected, and only the inclusion of the anisotropic signal of the bispectrum (the $P_{02} + B_{02}$ data-vector) grants significant improvement in the inference of the parameters $\{\alpha_{\parallel}, \alpha_{\perp}\}$, reducing the errorbars by 66 and 30% respectively—as in the previous case in Section 4.1.1.

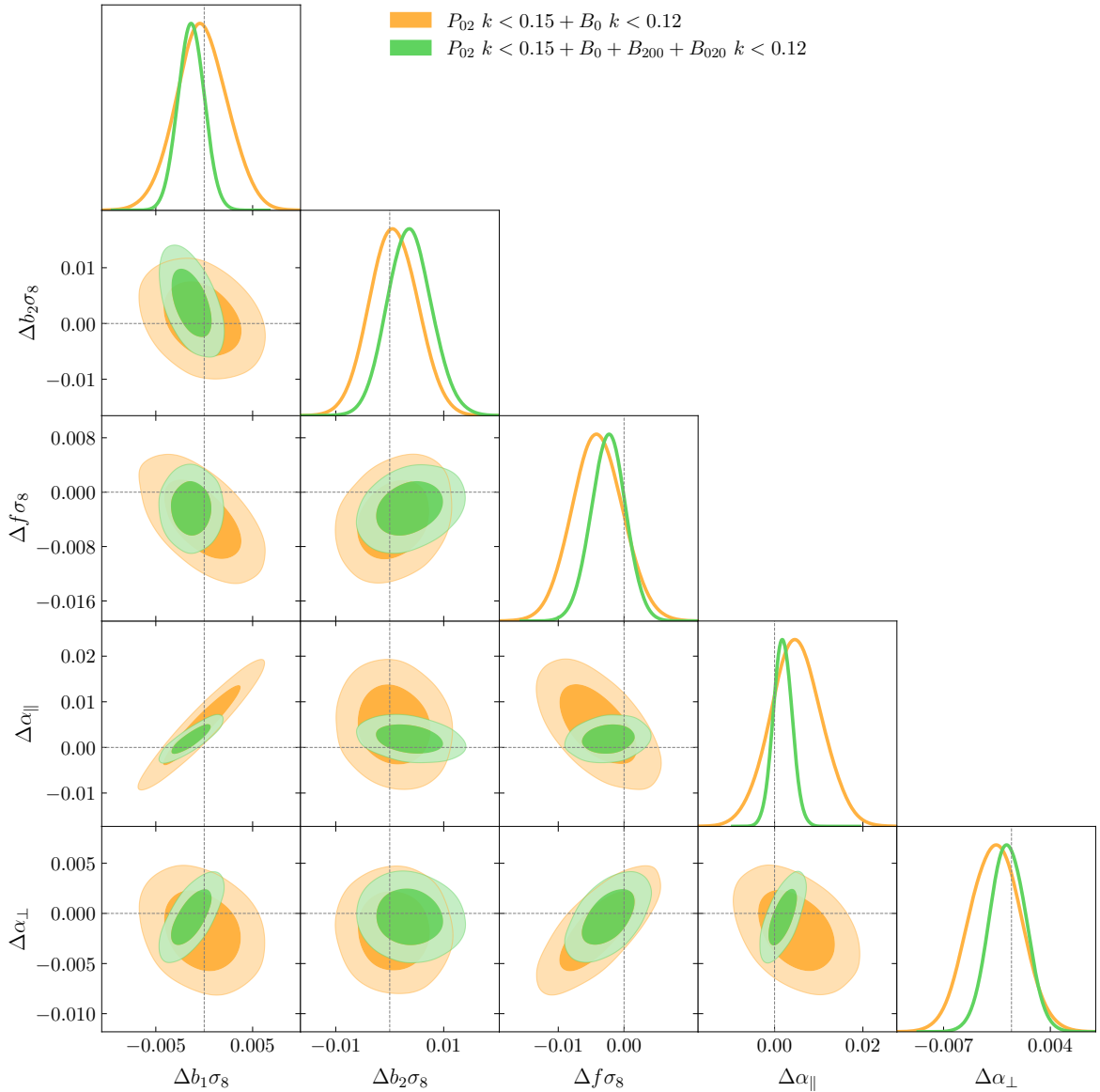


Figure 5. Main cosmological parameters recovered from the QUIJOTE fiducial dark matter simulations, using the (QUIJOTE)-calibrated effective Z_2^{GEO} kernel. The parameters are shown in terms of the deviation Δ from the fiducial (input) value. We show the cases where we use the combination of the power spectrum monopole and quadrupole (obtained as mentioned in 2) together with, respectively, B_0 and $B_0 + B_{200} + B_{020}$. The covariance is obtained from the simulations, and is rescaled to be equivalent to that of a volume of $100 \text{ (Gpc } h^{-1})^3$. As expected, using the bispectrum quadrupoles tightens the constraints significantly compared to the case with only B_0 . The FoG parameters, σ_P and σ_B , together with the deviations from Poissonian shot-noise A_P and A_B , are marginalized over.

There is a slight offset of $\sim 1.5\sigma$ in $f\sigma_8$ for $P_{02} + B_{02}$. The central value of the recovered $f\sigma_8$ is driven by the power spectrum part of the data-vector; the added value of the bispectrum is in breaking the $f\sigma_8$ degeneracy. Given this consideration and the large volume adopted here this bias does not invalidate the results of this paper, but this issue is further developed

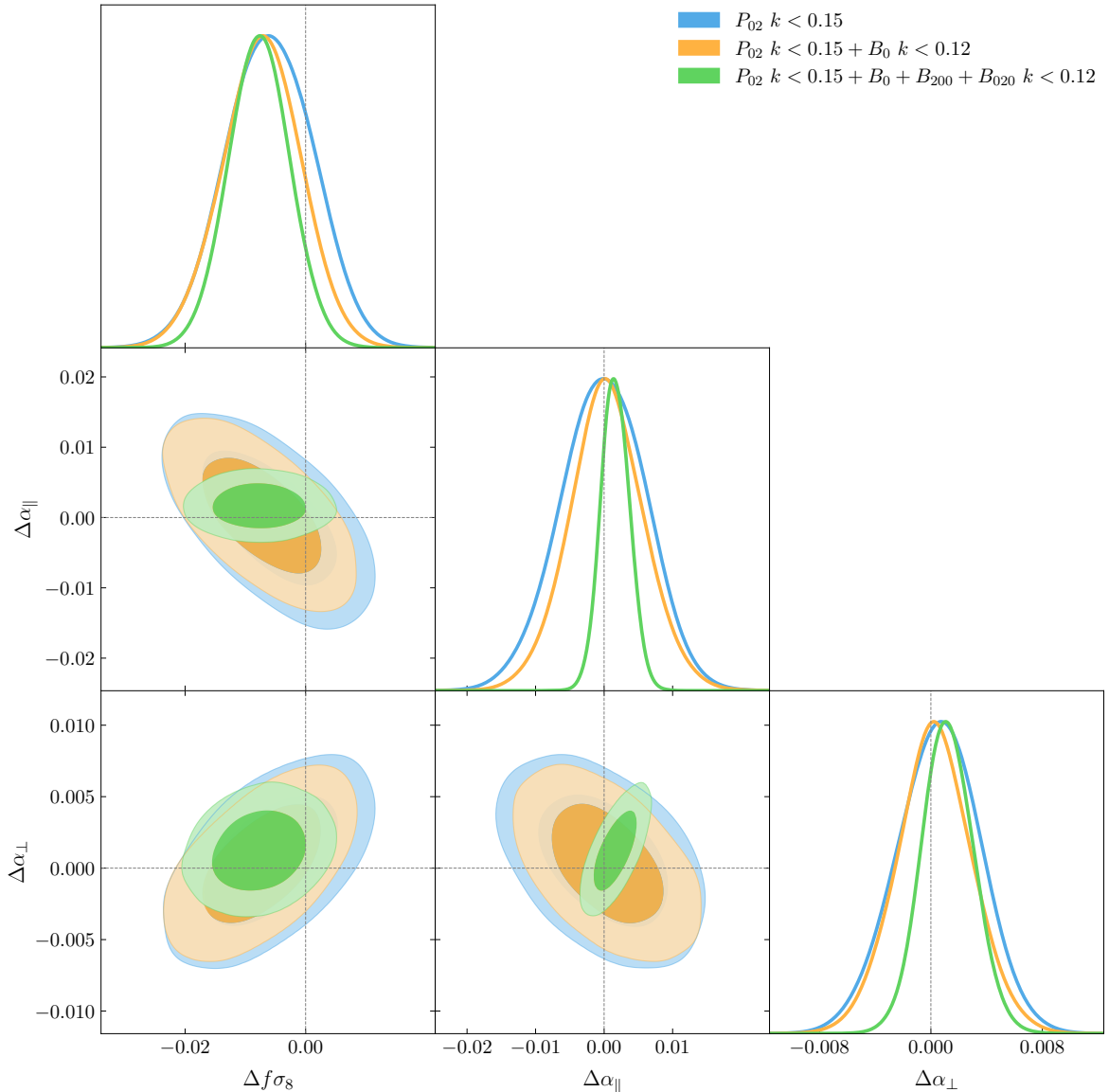


Figure 6. Main cosmological parameters recovered from the mean of the seven NSERIES halo and galaxy simulations, for the three sequential cases where, respectively, $P_0 + P_2$, $P_0 + P_2 + B_0$ and $P_0 + P_2 + B_0 + B_{200} + B_{020}$ are used. In this case, the covariance is estimated from the Patchy periodic box mocks, and is rescaled to match the physical volume of the signal, which corresponds to $123 (\text{Gpc } h^{-1})^3$. In this case, we use the non-local Lagrangian bias expansion, with b_1 and b_2 as free parameters, which we marginalize over together with the $\{\sigma_P, \sigma_B, A_P, A_B\}$ parameters.

in Section 4.2.

In short, we find that our analysis with the NSERIES galaxy simulations supports our claim that the bispectrum, with the modified Z_2^{GEO} kernel and paired with the local Lagrangian bias expansion specified in Eq. 2.7, is a solid approach to be adopted for large volume galaxy surveys. It does not bias the results relative to the power spectrum only analysis, and increases the precision in the inferred the Alcock-Paczyński parameters as well as

| Data-vector | $\Delta f \sigma_8 \pm 1\sigma$ | $\Delta \alpha_{\parallel} \pm 1\sigma$ | $\Delta \alpha_{\perp} \pm 1\sigma$ |
|----------------------------|---------------------------------|---|-------------------------------------|
| QUIJOTE DM simulations | | | |
| P_{02} | -0.0044 ± 0.0042 | 0.0027 ± 0.0063 | -0.0023 ± 0.0030 |
| $P_{02} + B_0$ | -0.0040 ± 0.0038 | 0.0047 ± 0.0057 | -0.0017 ± 0.0026 |
| $P_{02} + B_{02}$ | -0.0025 ± 0.0026 | 0.0018 ± 0.0021 | $(-4.4 \pm 18) \cdot 10^{-4}$ |
| NSERIES galaxy simulations | | | |
| P_{02} | -0.0060 ± 0.0073 | $(-8 \cdot 10^{-5}) \pm 0.00620$ | $(6.0 \pm 30) \cdot 10^{-4}$ |
| $P_{02} + B_0$ | -0.0072 ± 0.0065 | $(3.2 \pm 53) \cdot 10^{-4}$ | $(2.6 \pm 27) \cdot 10^{-4}$ |
| $P_{02} + B_{02}$ | -0.0077 ± 0.0051 | 0.0016 ± 0.0021 | 0.0012 ± 0.0018 |

Table 3. Performance in recovering the input cosmological parameters, for QUIJOTE and NSERIES, for the three choices of data-vector, $\{P_{02}, P_{02} + B_0, P_{02} + B_{02}\}$, where B_{02} denotes the combination $B_0 + B_{200} + B_{202}$. The errorbars correspond to the 1σ deviation for the effective volumes of, respectively, $100 (\text{Gpc } h^{-1})^3$ (QUIJOTE) and $80 (\text{Gpc } h^{-1})^3$ (NSERIES).

breaking the f - σ_8 degeneracy (see Section 4.2).

4.2 Disentangling the $f\sigma_8$ degeneracy

It is well known that the power spectrum data-vector is sensitive to the combination $f\sigma_8$: the two individual parameters f and σ_8 are highly correlated and thus cannot be separated in a reliable way with the power spectrum alone. This is the reason why in Section 4.1 we do not show the P_{02} results for f and σ_8 separately but only show the combination $f\sigma_8$.

In practice, with a large enough volume such as the one considered here, the power spectrum alone can break (weakly) the f and σ_8 degeneracy. We find, however, that with our adopted modeling for the power spectrum multipoles (and the adopted k_{max}), the recovered posterior distributions underestimate σ_8 while overestimating f , as Figure 7 and Table 4 show. The power spectrum 2σ regions for the two parameters are large – $\Delta\sigma_8 \sim 0.15$, $\Delta f \sim 0.2$ – because the additional constraining power arises only from the non-linear corrections. The fiducial values for f and σ_8 are recovered within 2σ only for $k_{\text{max}} \lesssim 0.12 h \text{ Mpc}^{-1}$. For higher values of the k_{max} of the power spectrum, k_{max}^P , the constraints obtained with P_{02} are biased. This effect is not limited to our approach and implementation: in fact it is consistent with the findings of [90–92].

This, along with a possible mild bias in the recovered central values of the combination $f\sigma_8$ which become appreciable only for very large volumes and in combination with the bispectrum, represents a serious limitation of the P_{02} modeling which should be corrected: in order to suitably extract the BAO feature (and thus infer the $\{\alpha_{\parallel}, \alpha_{\perp}\}$ parameters) from the power spectrum, mildly non-linear scales, up to at least $k \sim 0.15 h \text{ Mpc}^{-1}$ should be included. But state-of-the art modelling of P_{02} , for this choice of k_{max} and for large survey volumes, appears to introduce subtle parameters biases, especially on f and σ_8 . We leave further investigation of this to forthcoming works, as the focus of this paper is the model for the bispectrum. Nevertheless, since one of the central motivations for including the bispectrum in the analysis is precisely to disentangle the $f - \sigma_8$ degeneracy when combined with the power spectrum, we quantify the magnitude of the P_{02} -induced bias and its repercussions for the joint power spectrum-bispectrum analysis.

As Figure 7 and Table 4 show, when adding the bispectrum monopole to the data-vector, the peaks of the posterior distributions approach the true values. When the bispectrum quadrupoles are also included, in the $P_{02} + B_{02}$ case, the offset induced by the power spectrum

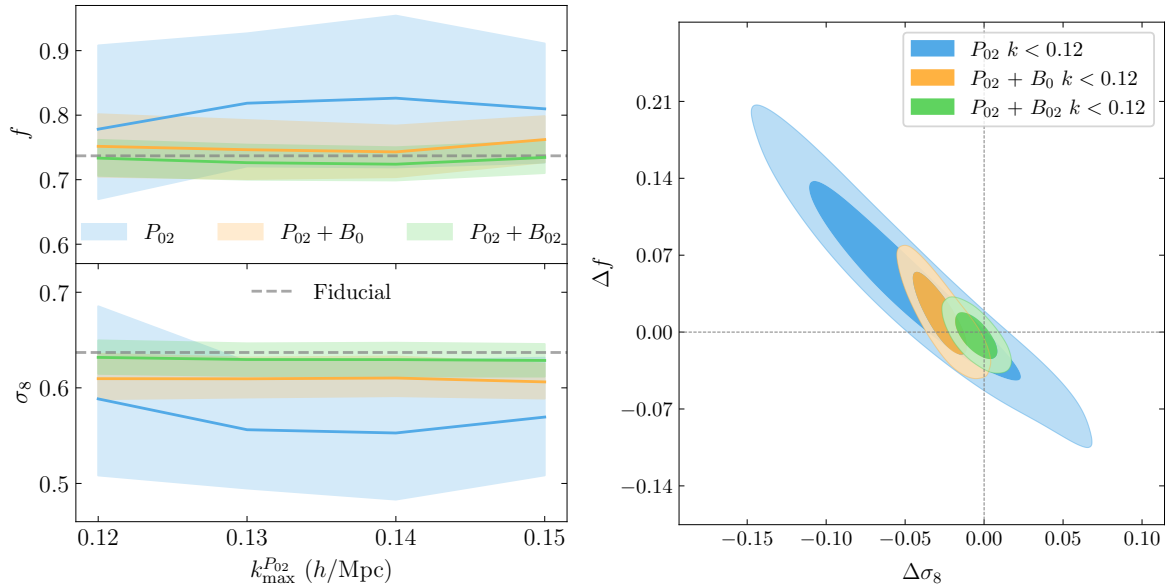


Figure 7. Left panel: Recovered f and σ_8 from the NSERIES galaxy simulations, as a function of the maximum k -vector considered in the P_{02} analysis, k_{\max}^P . Right panel: Marginalized f and σ_8 posteriors recovered with the NSERIES galaxy simulations, for $k_{\max}^P = k_{\max}^B = 0.12$. We show the results for the data-vectors $\{P_{02}, P_{02} + B_0, P_{02} + B_{02}\}$, and the errorbars correspond to an effective volume of ~ 80 ($\text{Gpc } h^{-1}$)³. The addition of the bispectrum monopole B_0 does not fully correct the bias induced by the power spectrum, while the full data-vector $P_{02} + B_{02}$ recovers the fiducial values for f and σ_8 , with errorbars markedly reduced.

| | $k_{\max}^{P_{02}} = 0.12$ | $k_{\max}^{P_{02}} = 0.13$ | $k_{\max}^{P_{02}} = 0.14$ | $k_{\max}^{P_{02}} = 0.15$ |
|-------------------------------|----------------------------|----------------------------|----------------------------|----------------------------|
| $\Delta \sigma_8 \pm 2\sigma$ | | | | |
| P_{02} | -0.049 ± 0.088 | -0.081 ± 0.066 | -0.084 ± 0.072 | -0.068 ± 0.062 |
| $P_{02} + B_0$ | -0.027 ± 0.024 | -0.028 ± 0.021 | -0.027 ± 0.020 | -0.031 ± 0.018 |
| $P_{02} + B_{02}$ | -0.005 ± 0.018 | -0.007 ± 0.017 | -0.007 ± 0.018 | -0.008 ± 0.017 |
| $\Delta f \pm 2\sigma$ | | | | |
| P_{02} | 0.04 ± 0.12 | 0.08 ± 0.10 | 0.09 ± 0.11 | 0.073 ± 0.092 |
| $P_{02} + B_0$ | 0.014 ± 0.048 | 0.010 ± 0.046 | 0.006 ± 0.040 | 0.025 ± 0.036 |
| $P_{02} + B_{02}$ | -0.004 ± 0.028 | -0.011 ± 0.027 | -0.013 ± 0.026 | -0.003 ± 0.025 |

Table 4. Recovered constraints for the parameters σ_8 (upper panel) and f (lower panel) for the NSERIES simulations, as a function of k_{\max}^P , while k_{\max}^B is fixed to 0.12. We display the three choices of data-vector $\{P_{02}, P_{02} + B_0, P_{02} + B_{02}\}$, where, as stated throughout the paper, P_{02} and B_{02} denote the combinations $P_0 + P_2$ and $B_0 + B_{200} + B_{020}$ respectively. The errorbars correspond to the 2σ deviation for the NSERIES effective volume, 80 ($\text{Gpc } h^{-1}$)³.

is fully corrected. This offers a further motivation for utilizing the full $B_{02} = B_0 + B_{200} + B_{020}$ data-vector.

4.2.1 Additional considerations and robustness tests

A possible source of error in the power spectrum modeling could be the integration of the loop terms. In theory the range of the integrals in the 1 and 2-loop terms is from $k = 0$

to infinity, while in practice we use a reasonable upper cutoff scale of $k = 1 h \text{ Mpc}^{-1}$. We investigate whether increasing the cutoff scale affects the recovered parameters in Appendix C. There, we show that this effect is absorbed by the nuisance parameter $\sigma_{\mathcal{P}}$, so we confirm that for this application, this approximation is adequate and does not introduce bias in the analysis.

Moreover, while we fit the bispectrum kernel to the data vector of bispectrum monopole and quadrupoles, parameters biases could be introduced if redshift space distortions induced a preference for different kernel parameters of Equation 2.16 between the bispectrum monopole and quadrupoles. We explore this extension, which we refer to as ‘2-kernels’ modification, in Appendix C where we conclude that this preference is not significant; hence we do not consider further any of the ‘2-kernels’ modifications, which we consider would be over-fitting.

4.3 Testing strong growth factor variations

We use the CW simulations to explore the performance of the GEO-FPT model with Λ CDM cosmologies featuring significantly different values of Ω_m from the ones where the kernels have been calibrated. This effectively tests the model’s performance for significantly different growth factors.

The single CW simulations with matter densities $\Omega_m = \{0.2, 0.27, 0.4, 1.0\}$ feature the same initial conditions¹⁸. As further discussed in Appendix B, the CW simulations are only sufficiently accurate to study relative effects (variations with respect to the fiducial, $\Omega_m = 0.27$ simulation) and only up to $k_{\text{max}} = 0.11$.

We perform cosmological parameters inference with the QUIJOTE-calibrated GEO-FPT bispectrum, for each of the single simulations that share the same initial conditions, using the more conservative value of $k_{\text{max}} = 0.11$. In all cases, we adopt the covariance estimated from the fiducial set of QUIJOTE simulations; this assumes, as usually done, that the covariance does not change radically with cosmology.

The maximum likelihood parameters, relative to those of the fiducial simulation, are shown in Figure 8. There is an increase of systematic errors with distance from the fiducial case (where the cosmology is closest to the QUIJOTE simulations). The systematic shifts in the various combinations of the AP parameters are driven by the power spectrum, but are below 0.3% except, not unexpectedly, for $\Omega_m = 1$, where they grow to 1%. The deviations on the $f\sigma_8$ parameter are within 1% in the cases with $\Omega_m = 0.2 - 0.4$ for all data-vectors, and are also driven by the power spectrum. As seen in Section 4.2, the full data-vector $P_{02} + B_{02}$ helps breaking the $f - \sigma_8$ degeneracy correctly, reducing the bias driven by P_{02} . This bias remains below 2% even at $\Omega_m = 1$.

While not unexpected, given that the SPT bispectrum kernels have a very weak cosmology dependence, these tests demonstrate that GEO-FPT bispectrum (calibrated on a fiducial cosmology) works well even for cosmologies that deviate from the Planck-preferred one. The small residual biases (which only become visible for such large volumes) appear to be driven by limitations in the modeling of the power spectrum.

5 Conclusions

Higher-order statistics such as the bispectrum are promising tools to extract cosmological information beyond that encoded in the power spectrum. Having an accurate enough bis-

¹⁸For the fiducial cosmology with $\Omega_m = 0.27$ there are 160 simulations in total, of which one has the same initial conditions as for the other cosmologies.

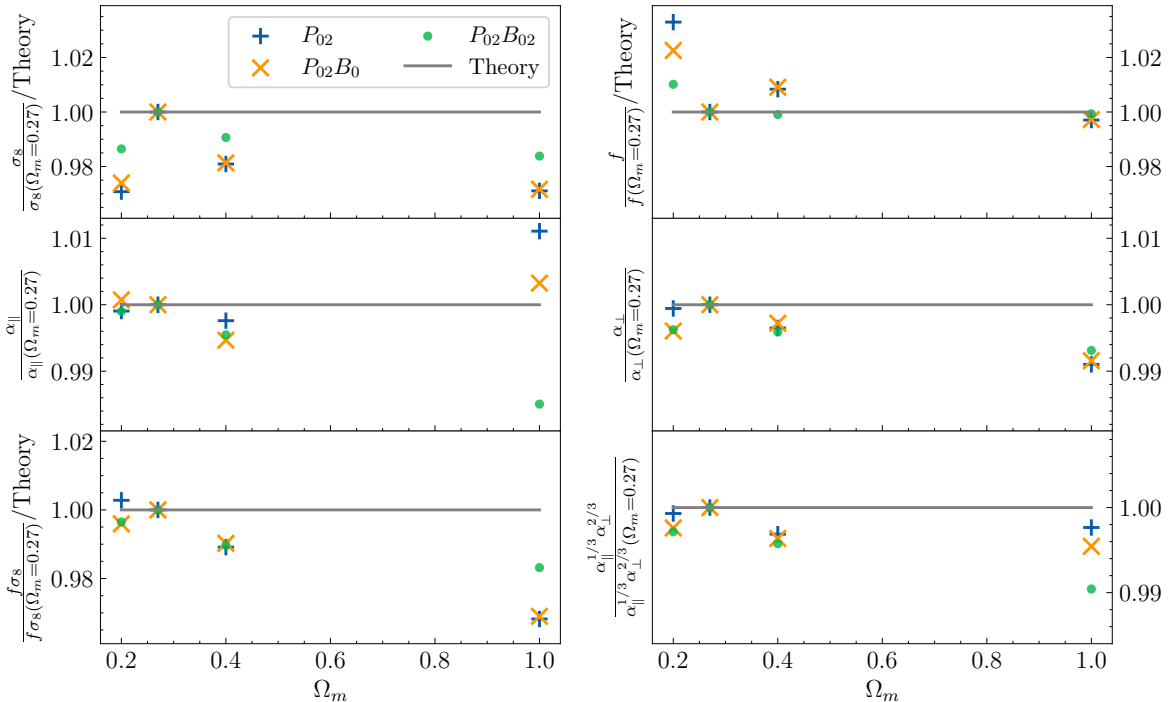


Figure 8. Increase of systematic errors as a function of distance from the fiducial $\Omega_m = 0.27$ case –where the cosmology is closest to the QUIJOTE simulations, in which the bispectrum effective kernel Z_2^{GEO} has been calibrated. The parameters are inferred from the dark matter CW simulations for $\Omega_m = 0.2, 0.27, 0.4, 1$, one box of $(2.4\text{Gpc } h^{-1})^3$ each. The recovered parameters ratios (to the fiducial cosmology simulation) are normalized by the theoretical value in the case of f , σ_8 and $f\sigma_8$ for clarity. As seen before, when f and σ_8 are treated as independent parameters, the bias in the recovered values is driven by the power spectrum.

pectrum model is one of the main challenges that an analysis of the bispectrum of a galaxy redshift survey involves.

We have presented the GEO-FPT model for the redshift space bispectrum monopole and quadrupoles. GEO-FPT is a phenomenological modification of the tree-level SPT bispectrum consisting in a modulation of the Z_2 SPT kernel by a function with 5 free parameters that we have calibrated on the QUIJOTE dark matter simulations for a k -range of $0.02 < k[h\text{Mpc}^{-1}] < 0.12$, and redshift range $z = 0.5 - 2.0$. This k -range provides access to the information contained in the mildly non-linear regime. In the k -range of interest, GEO-FPT reproduces the bispectrum monopole from N-body simulations at $\lesssim 3\%$ level, and the quadrupoles at $\lesssim 30\%$, well within the 1σ statistical errors for a survey volume of $100 (\text{Gpc } h^{-1})^3$.

The GEO-FPT performance in recovering the cosmological parameters $\{\sigma_8, f, \alpha_{\parallel}, \alpha_{\perp}\}$, is validated in three different sets of synthetic catalogs: the same QUIJOTE simulations where it had been calibrated; the NSERIES galaxy simulations, featuring a WMAP-compatible cosmology; and the CW dark matter simulations, with values of $\Omega_m = 0.2, 0.27, 0.4, 1$, at fixed $\Omega_m h^2$. GEO-FPT provides a markedly improved performance (in terms of accuracy and k -range) compared to other state-of-the-art bispectrum models.

Both the QUIJOTE and NSERIES analyses are carried out for effective volumes of 100 and

80 $(\text{Gpc } h^{-1})^3$ respectively, far exceeding the target of upcoming surveys. This is a stringent test for the systematic errors of the GEO-FPT model, which recovers the cosmological parameters within the narrow statistical error correspondent to the adopted cosmological volume. In particular, the NSERIES results show that the GEO-FPT model is readily applicable to biased tracers, such as galaxies and quasars. The test on the CW simulations (which feature strongly different growth factors and Ω_m) further confirms that the GEO-FPT model remains valid for a wide range of cosmologies.

Including the bispectrum monopole and quadrupoles in a joint analysis with the power spectrum monopole and quadrupole not only improves dramatically the errorbars on α_{\parallel} and α_{\perp} (reducing them by respectively 66 and 30%), but also breaks the $f - \sigma_8$ quasi-degeneracy present in the power spectrum. The state-of-the-art modeling of the anisotropic galaxy power spectrum in redshift space used here is shown to be the main limitation in recovering unbiased estimates for the individual f and σ_8 parameters. This should be an important objective of future work. In view of an application to forthcoming galaxy surveys, further work is also needed to develop a suitable modeling on the survey window function on the galaxy bispectrum monopole and quadrupoles (see e.g. [93, 94] for pioneering efforts in this direction).

The calibrated model and related data vectors and covariances are made publicly available at <https://github.com/serginovell/Geo-FPT>. Two options are provided: a calibration in view of the use of the full bispectrum monopole and quadrupoles data vector and one that includes the bispectrum monopole only, for cases where the inclusion of the multipoles is unfeasible.

Acknowledgements

SNM acknowledges funding from the official doctoral program of the University of Barcelona for the development of a research project under the PREDOCS-UB grant. HGM acknowledges support through the program Ramón y Cajal (RYC-2021-034104) of the Spanish Ministry of Science and Innovation. LV, DG and HGM acknowledge support of European Union’s Horizon 2020 research and innovation programme ERC (BePreSySe, grant agreement 725327).

Funding for this work was partially provided by the Spanish MINECO under project PGC2018-098866-B-I00MCIN/AEI/10.13039/501100011033 y FEDER “Una manera de hacer Europa”, and the “Center of Excellence Maria de Maeztu 2020-2023” award to the ICCUB (CEX2019-000918-M funded by MCIN/AEI/10.13039/501100011033).

This work has made extensive use of the following publicly available codes: [CLASS](#), [EMCEE](#), [PTCOOL](#), [GSL](#), [RUSTICO](#), [SCIPLY](#), [NUMPY](#), [GETDIST](#), [MATPLOTLIB](#), [FFTW](#). We are grateful to the developers who made these codes public.

A Covariance matrix estimation and results

Throughout this work, all the covariance matrices have been estimated from simulations in the traditional way as follows. Let \mathbf{D} be the data-vector of interest, \mathbf{D}_i be the measured data-vector in the i -th simulation, and n the number of simulations. The covariance matrix \mathbf{C} is obtained as

$$\mathbf{C} = \frac{1}{n-1} \sum_{i=1}^n (\mathbf{D}_i - \bar{\mathbf{D}})(\mathbf{D}_i - \bar{\mathbf{D}})^T, \quad (\text{A.1})$$

where $\overline{\mathbf{D}}$ is the mean across all realizations,

$$\overline{\mathbf{D}} = \frac{1}{n} \sum_{i=1}^n \mathbf{D}_i. \quad (\text{A.2})$$

The reduced covariance matrix of the bispectrum data-vector used in this work is plotted in Figure 2. For completeness, we show in Figure 9 the covariance matrix for the full data-vector used in the cosmological parameter inference plus the B_{002} multipole, which includes the auto and cross terms involving the power spectrum monopole and quadrupoles. The left panel illustrates the fine details of the full structure of the covariance matrix, while the right panel quantifies the auto and cross-correlations in blocks by showing the median value of all coefficients in the corresponding box. The values correspond to the reduced covariance matrix, so that the terms concerning the power spectrum and bispectrum have comparable value. Of course, this is an extreme compression of all the information present in the covariance matrix, but it qualitatively illustrates the importance of the cross-correlations compared with the corresponding auto-correlations.

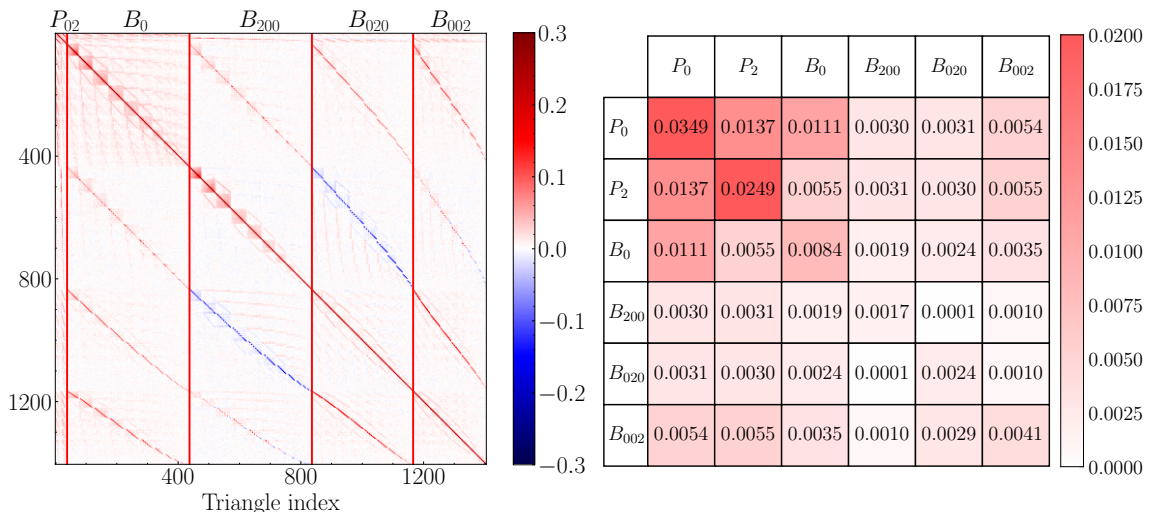


Figure 9. Left panel: reduced covariance matrix of the data-vector formed by $\{P_0, P_2, B_0, B_{200}, B_{020}, B_{002}\}$ at $z = 0.5$: extended version of Figure 2. Together with the structure within the bispectrum data-vector, we can observe how the power spectrum is clearly correlated with the bispectrum, especially with the bispectrum monopole B_0 . Right panel: median of all correlation terms between each pair of data-vectors. At each cell, we show the median value of all the elements in the box of the reduced covariance matrix that relate the data-vectors in the corresponding row and column.

The errorbars that result from using a covariance estimated with n simulations correspond to an equivalent volume of one such simulation, V_{sim} . When doing parameter inference, if we use the mean of n simulations as the measured data-vector, this signal corresponds to that of the cumulative volume covered by the n simulations. In fitting the free parameters of our formula, $\{f_1, \dots, f_5\}$, we rescale the estimated covariance matrix by a factor of n , thus effectively transforming the errorbars from corresponding to a volume of V_{sim} to $n \times V_{\text{sim}}$.

In particular, when fitting $\{f_1, \dots, f_5\}$ we rescale the covariance estimated with the QUIJOTE simulations by the number of realizations at each redshift, 8000 at $z = 0.5$ and 4000 at $z = 1, 2$. These errorbars can be seen in Figures 3, 11.

It is only in the cosmological parameter recovery in the QUIJOTE sims, in Figures 5 and 12 (right panel), that we opt for rescaling the covariance by a factor different than the number of simulations. In particular we set $n = 100$ in this case, corresponding to a volume of $100 (\text{Gpc } h^{-1})^3$.

Similarly, in doing the cosmological parameter exploration for NSERIES (Figures 6, 13), we rescale the covariance by a factor of 7, to obtain errorbars for an equivalent physical volume of $7 \times (2.6 \text{ Gpc } h^{-1})^3 = 123 (\text{Gpc } h^{-1})^3$ (effective volume of $80 (\text{Gpc } h^{-1})^3$). We compute the effective volume from a given physical volume as in [76]. This is in line of the main goal of this paper, which is to show that our proposed model is appropriate for cosmological volumes $\leq 100 (\text{Gpc } h^{-1})^3$.

We use the covariance obtained with QUIJOTE also for the analysis performed on the CW simulations, assuming that the covariance does not strongly depend on cosmology. To match the volume of each CW realization, we rescale the covariance by $n = \left(L_{\text{box}}^{\text{CW}}/L_{\text{box}}^{\text{Quijote}}\right)^3$. This is however of negligible importance for the role of the CW simulations in this paper, since we only consider the ratios between maximum likelihood parameters, as seen in Section 4.3.

B QUIJOTE complementary results

In Figure 10 a comparison between the model presented in this paper (GEO-FPT, Eq. 2.6), and the standard tree-level Standard Perturbation Theory (SPT, Eq. 2.17) is shown. Such comparison is presented as a function of the triangle area for $z = 0.5$ for the bispectrum monopole (top panel), similarly to what was already shown in Figure 1 of Section 2, as a function of the triangle index for $z = 0.5, 1, 2$, and for the bispectrum monopole and quadrupoles, as indicated (bottom panels). We report a substantial improvement of the performance of the GEO-FPT model over SPT model for the explored triangle configurations ($k_i \leq 0.12 h \text{ Mpc}^{-1}$). This improvement is increasingly evident with increasing area of the triangle (in Fourier space). This is the expected trend; when the area of the k -triangle increases, also the k -sides increase, corresponding to smaller scales, where the tree-level SPT model is expected to fail more dramatically. These improvements can be quantified by the χ^2 values, as reported in the legend. As in Figure 1, the grey band displays the 1σ error corresponding to a volume of $100 \text{ Gpc } h^{-1}$, where the \hat{B}_0 signal comes from a total volume of $8000 (\text{Gpc } h^{-1})^3$.

In the following subsections we address the power suppression effect between theory and simulations (Appendix B.1) and quantify the effect of P_{02} in the recovered constraints with QUIJOTE for $z = 1, 2$ when the $f - \sigma_8$ degeneracy is broken (Appendix B.2).

B.1 Comparison Quijote-CW simulations

It is well known that N-body simulations feature a loss of power at small scales, dependent on the initial conditions redshift z_{ini} and the time-stepping/mass resolution [68–70]. In the left panel of Figure 11 we quantify how this affects the non-linear matter power spectrum, which is indicative as well of its effect on higher-order statistics such as the bispectrum. The Figure shows the ratio $P_{\text{measured}}/P_{\text{theory}}$, where P_{measured} is the estimated quantity from the real space simulations and P_{theory} is computed for the fiducial model following Equation 2.1.

This power suppression in the power spectrum, which is stronger at higher redshifts and for the CW simulations, is visible, possibly due to CW having a lower initial conditions redshift and different resolution/time-stepping settings. While for the QUIJOTE simulations

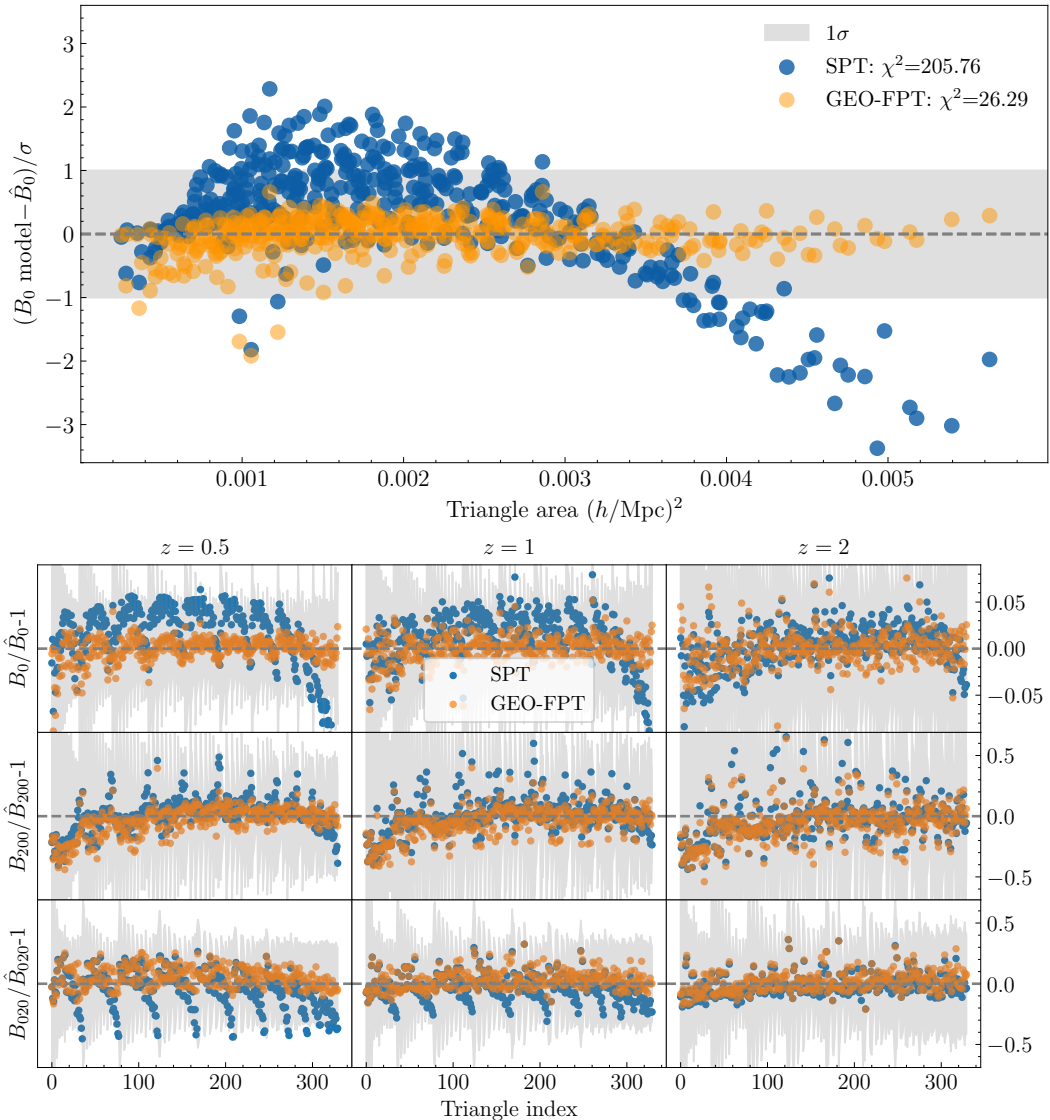


Figure 10. Performance of GEO-FPT (orange symbols) and tree-level SPT (blue symbols) in describing the measured bispectrum monopole signal in the dark matter QUIJOTE simulations. The upper panel is similar to that shown in the lower panel of Figure 1, where the difference between bispectrum model and measurements is shown as a function of the triangle area (each dot in the figure corresponds to a bispectrum triangle). In this case we only display the $z = 0.5$ outputs for clarity. The total number of configurations is 399 for triangles with $k_i \leq 0.12 h \text{ Mpc}^{-1}$, binned such that $\Delta k_i = 1.1 k_i$. For the tree-level SPT model only the FoG damping term is freely varied, and consequently the number of degrees of freedom is $399 - 1$; whereas for the GEO-FPT 5 additional f_i parameters (see Table 2) have been calibrated to these simulations, the number of degrees of freedom is $399 - 6$. The reported χ^2 values in the legend correspond to a covariance with an associated effective volume of $100 \text{ Gpc } h^{-1}$, whereas the signal has an associated volume of $8000 \text{ Gpc } h^{-1}$, hence the ‘low’ χ^2 in both cases. The lower panels are analogous to the right panels in Figure 2, where the comparison is for the multipoles B_0, B_{200}, B_{020} for the redshifts $z = 0.5, 1, 2$. The GEO-FPT model shows a much better agreement with the simulated data even considering the additional adjustable parameters of the model.

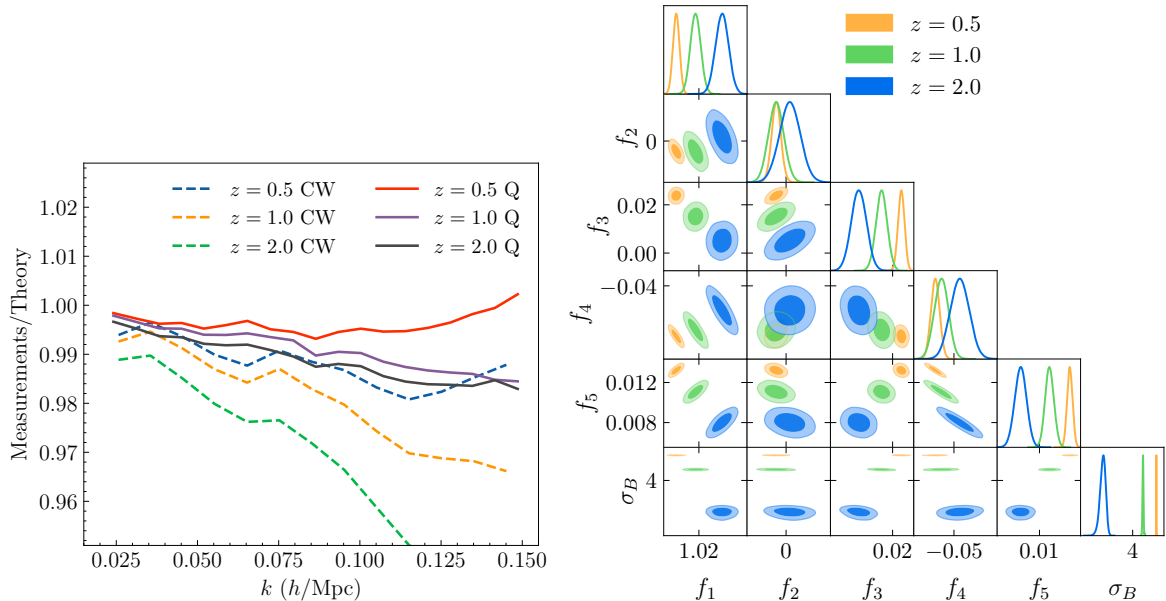


Figure 11. Left panel: Loss of power of both QUIJOTE and CW simulations, at $z = 0.5, 1, 2$. The ratios between theoretical and measured non-linear matter power spectrum are shown. The theoretical model is 2L-RPT, as in the main analysis, computed for the simulation cosmology. While in the case of QUIJOTE the loss of power is almost always $< 1\%$, in the case of CW the effect is much larger especially at $z=1$ and 2 and at $k \gtrsim 0.1$ at $z = 0.5$. Right panel: Posterior distributions for the calibration of the Z_2^{GEO} kernels at the three redshifts of interest, $z = 0.5, 1, 2$, where the covariance has been rescaled to match the full volume of the signal ($8000 \text{ (Gpc } h^{-1})^3$ at $z = 0.5$ and $4000 \text{ (Gpc } h^{-1})^3$ at $z = 1, 2$). This is complementary to Figure 3, since this Figure shows the parameters’ correlations. The strongest correlation is between f_1, f_4, f_5 , while f_3 appears to be very orthogonal to the other parameters, as well as the nuisance parameter σ_B (as expected).

the loss of power is contained within 1% for the k -range used in the bispectrum analysis, the CW measurement of the matter power spectrum at $z = 0.5$ is already deviating 1% from the theory at $k = 0.08 \text{ h Mpc}^{-1}$. This worsens with k and redshift.

Systematic errors of this magnitude have been acceptable until the recent past, as they were below the statistical errors. However, in this work, given the large volume considered ($\sim 100 \text{ (Gpc } h^{-1})^3$), the effects of this power suppression may become relevant. The power suppression of the CW simulations precludes us from repeating a similar analysis to that of Sections 4.1.1 and 4.1.2. Therefore, instead of evaluating the recovered cosmological parameter posteriors of every case separately, in Section 4.3 we show the results at each cosmology relative to those for the fiducial one, while setting a more conservative k -range of $0.02 < k[\text{h Mpc}^{-1}] < 0.11$ for the bispectrum.

B.2 Further details on the posterior distributions for QUIJOTE simulations

The right panel of Figure 11 shows the posterior distributions for the kernel parameters $\{f_1, \dots, f_5\}$, obtained as described in Section 3. The degeneracies between each pair of parameters are now visible, with the $f_1 - f_4 - f_5$ degeneracy being the most apparent.

In the left panel of Figure 12, we show the 2D constraints for f and σ_8 at $z = 0.5$ for the data-vectors $\{P_{02}, P_{02} + B_0, P_{02} + B_{02}\}$. As in Section 4.1.1, the adopted maximum

k-vectors are $k_{\max}^P = 0.15$ for the power spectrum and $k_{\max}^B = 0.12$ for the bispectrum. For a distribution of dark matter tracers, all constraints are unbiased at $\sim 1\sigma$ level for a volume of $100 (\text{Gpc } h^{-1})^3$. Comparison with Section 4.2 indicates that the bias in these parameters seen in the NSERIES galaxy mocks can be due to the combination of the following two effects. Compared to QUIJOTE, NSERIES simulates biased tracers. Also, the true statistical errors in QUIJOTE are the ones corresponding to the mean signal, which is that of a volume of $8000 (\text{Gpc } h^{-1})^3$, while the statistical error of NSERIES corresponds to a volume 100 times smaller. Hence, the bias we see in P_{02} in NSERIES could just be a 2σ statistical fluctuation.

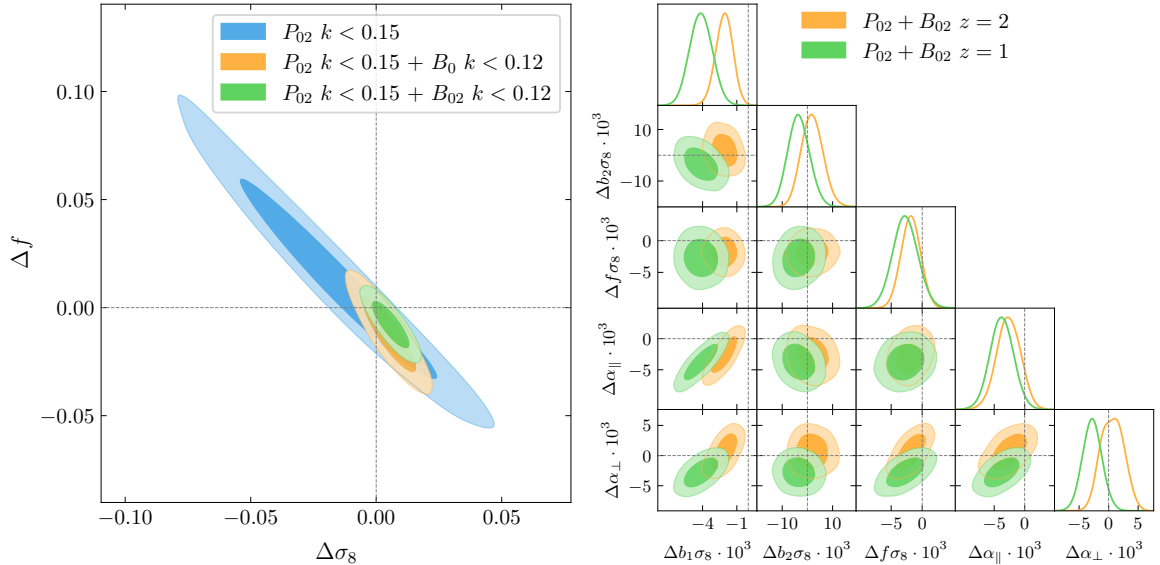


Figure 12. Left panel: 2D posterior distribution for the pair of parameters f and σ_8 for the QUIJOTE simulations at $z = 0.5$. Differently than in Figure 7 (NSERIES galaxy mocks), the result for QUIJOTE simulations is unbiased for both the power spectrum and the combined power spectrum-bispectrum data-vectors. Right panel: Main cosmological parameters recovered from the QUIJOTE fiducial simulations, at redshifts $z = 1, 2$, with the variables multiplied by 10^3 . All settings are as in Figure 5, except that here for the two redshift snapshots we show results for the full data vector.

In the right panel of Figure 12, we display the cosmological parameter fit for QUIJOTE at redshifts $z = 1, 2$, with the Z_2^{GEO} kernel fixed at the best-fit coefficients fitted at the corresponding redshifts (Table 2). While the cosmology is broadly recovered, the accuracy is worse than at $z = 0.5$ (Section 4.1.1). We attribute this effect in large part to the power spectrum data-vector P_{02} , which is more affected by small-scales loss of power at $k \gtrsim 0.12 h \text{ Mpc}^{-1}$ than at lower redshift.

We further quantify the importance of developing and adopting a more accurate model for the power spectrum in Table 5. There we report the $\Delta\chi^2$ between the data vector for the best fit and that for the fiducial parameters for the three redshifts of interest in QUIJOTE, $z = 0.5, 1, 2$. What we refer as “fiducial” are the parameters that are shown as a dashed line in Figures 12 and 5: namely, the σ_8 and f values as computed by CLASS for the given cosmology and redshift; the bias parameters $b_1 = 1, b_2 = 0$; the shot-noise parameters $A_P = A_B = 1$; the σ_P, σ_B are the (conditional¹⁹) best fit to the simulations data. The table shows that the shift in χ^2 induced by B_{02} is minuscule compared to that induced by P_{02} considering the

¹⁹With the previous parameters fixed at the fiducial values.

number of bispectrum configurations: the power spectrum has a very strong preference for the biased cosmological parameters and is driving the offsets seen in Figures 12 and 5. This is important, but goes beyond the scope of this paper and will be addressed elsewhere.

| QUIJOTE $\Delta\chi^2$ respect to fiducial | | | |
|--|-----------|---------|---------|
| Covariance terms | $z = 0.5$ | $z = 1$ | $z = 2$ |
| P_{02} | -87.26 | -286.07 | -295.90 |
| B_{02} | -9.84 | -2.03 | -2.57 |
| $P_{02} + B_{02}$ | -174.98 | -478.86 | -481.52 |
| Off-diagonal | -77.88 | -190.76 | -183.05 |

Table 5. Difference in χ^2 between the best-fit and the fiducial cosmological parameters for the QUIJOTE simulations at $z = 0.5, 1, 2$. The fiducial cosmological parameters are the σ_8 and f corresponding to each redshift; $b_1 = 1, b_2 = 0, A_P = A_B = 0$; and σ_P, σ_B obtained as the best fit for the full $P_{02} + B_{02}$ data-vector considering the remaining parameters fixed at their fiducial values. In each row we display the values corresponding to different parts of the data-vector, which correspond to different blocks of the covariance matrix: the P_{02} block, the B_{02} block, the full covariance matrix ($P_{02} + B_{02}$), and the off-diagonal contribution. The B_{02} shift in χ^2 is much smaller than that of the P_{02} indicating that the power spectrum has a very strong preference for the biased cosmological parameters but not the bispectrum. This confirms that the power spectrum is driving the offsets seen in Figures 12 and 5 (where for the lower redshift $z = 0.5$ the offsets are much less pronounced).

C NSERIES complementary results

We assess here the performance of the “2-kernels” extension of Equation 2.16 which modifies the Z_2^{GEO} kernels by introducing 5 extra free coefficients $\{g_1, g_2, g_3, g_4, g_5\}$:

$$Z_2^{\text{GEO}} \rightarrow Z_2^{\text{SPT}} \times \left[(f_1 + \ell g_1) + (f_2 + \ell g_2) \frac{\cos(\theta_{\text{med}})}{\cos(\theta_{\text{max}})} + (f_3 + \ell g_3) \frac{\cos(\theta_{\text{min}})}{\cos(\theta_{\text{max}})} + (f_4 + \ell g_4) \frac{A}{A_{\text{norm}}} + (f_5 + \ell g_5) \frac{A^2}{A_{\text{norm}}} \right], \quad (\text{C.1})$$

where $\ell = 0$ for the bispectrum monopole and $\ell = 1$ for the quadrupoles. The first set of parameters, $\{f_1, \dots, f_7, \sigma_B\}$, is adjusted to the B_0 QUIJOTE measurements. Then, keeping their values fixed at the best fit, the $\{g_1, \dots, g_5\}$ parameters values (which are only activated when $\ell \neq 0$) are fitted to the $B_0 + B_{200}$ QUIJOTE measurements.

In this way, the f_i parameters are optimized for the bispectrum monopole, while the g_i parameters quantify the discrepancy between the best functional form for the monopole and that for the quadrupoles. As such, we should expect some improvement in the accuracy of the constraints of cosmological parameters.

As shown in Figure 13, the improvement is minimal for our data-vector of interest, $P_{02} + B_{02}$. For this reason the 2-kernels extension of Equation C.1 is not considered in the main text of the paper. This finding indicates that our adopted baseline model does not perform significantly better in some multipoles than in others.

Nonetheless, when using only the $P_{02} + B_0$ data vector, the 2-kernels modification (i.e., fitting the eq. 2.16 kernel parameters only to B_0) improves the recovery of the individual f and σ_8 parameters. We recognize that this modification can be suitable in cases where adding the quadrupoles is unfeasible and only the $P_{02} + B_0$ data vector is available. However, considering

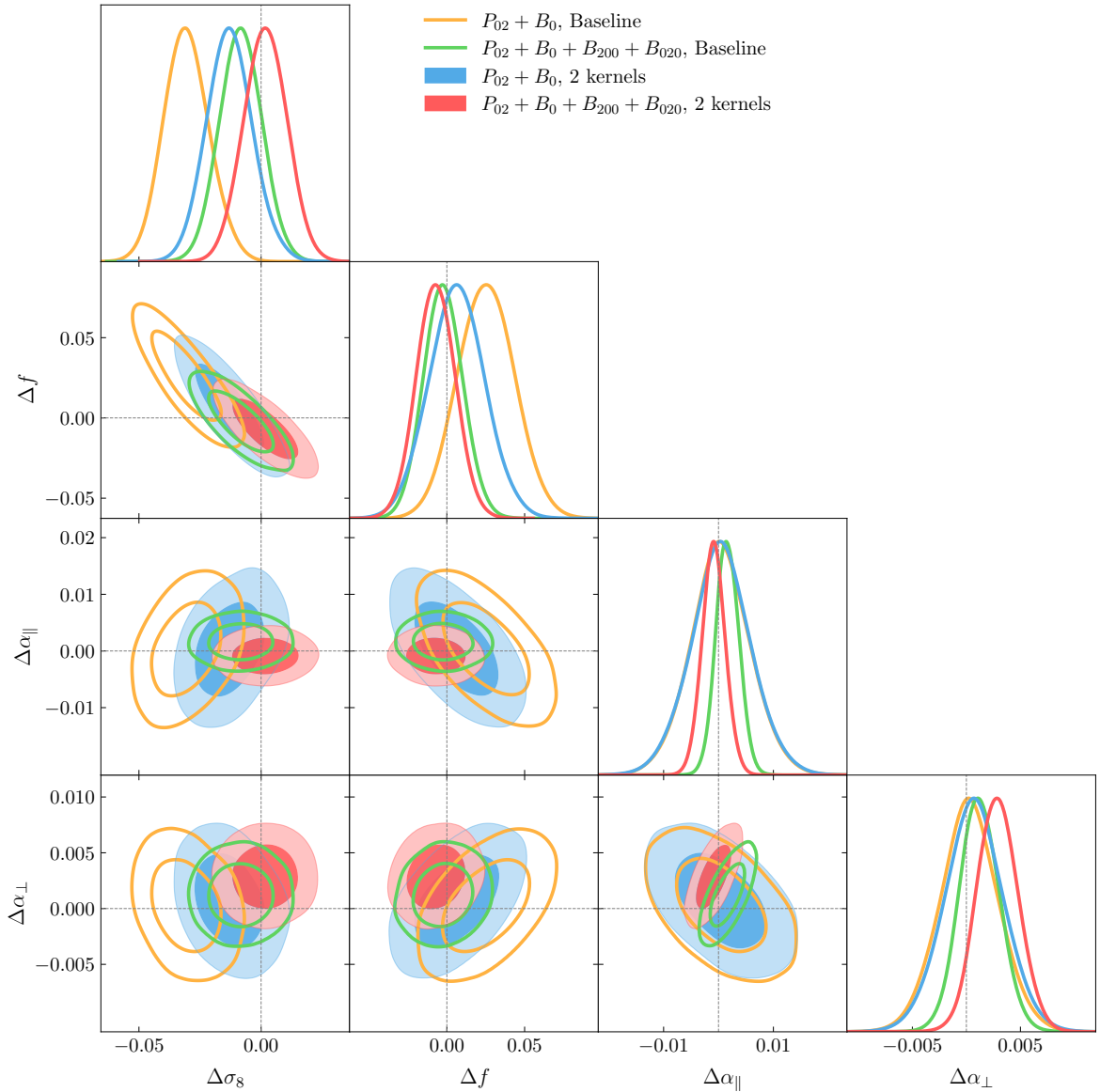


Figure 13. Comparison of the approaches presented in Equation 2.16 (baseline, being the same as in Figure 6) and Equation C.1 (2 kernels) for the data-vectors $P_0 + P_2 + B_0$ and $P_0 + P_2 + B_0 + B_{200} + B_{020}$.

that, as shown in Section 4.2, the offset in the f and σ_8 parameters is mainly caused by the power spectrum, the improvement seen in the 2-kernels case for the $P_{02} + B_0$ data-vector may be spurious. Nevertheless, we provide the option to use the B_0 -fitted f_i parameters in the released code.

Finally, we display in Figure 14 the behaviour of the P_{02} -recovered parameters f , σ_8 and the nuisance parameter σ_P , depending on the value of the cutoff k of the integrals for the loop terms of the power spectrum. We clearly observe how the effect of increasing the cutoff k is absorbed by the FoG nuisance parameter σ_P , thus discarding the specific choice of cutoff k as the source for the bias in disentangling f and σ_8 .

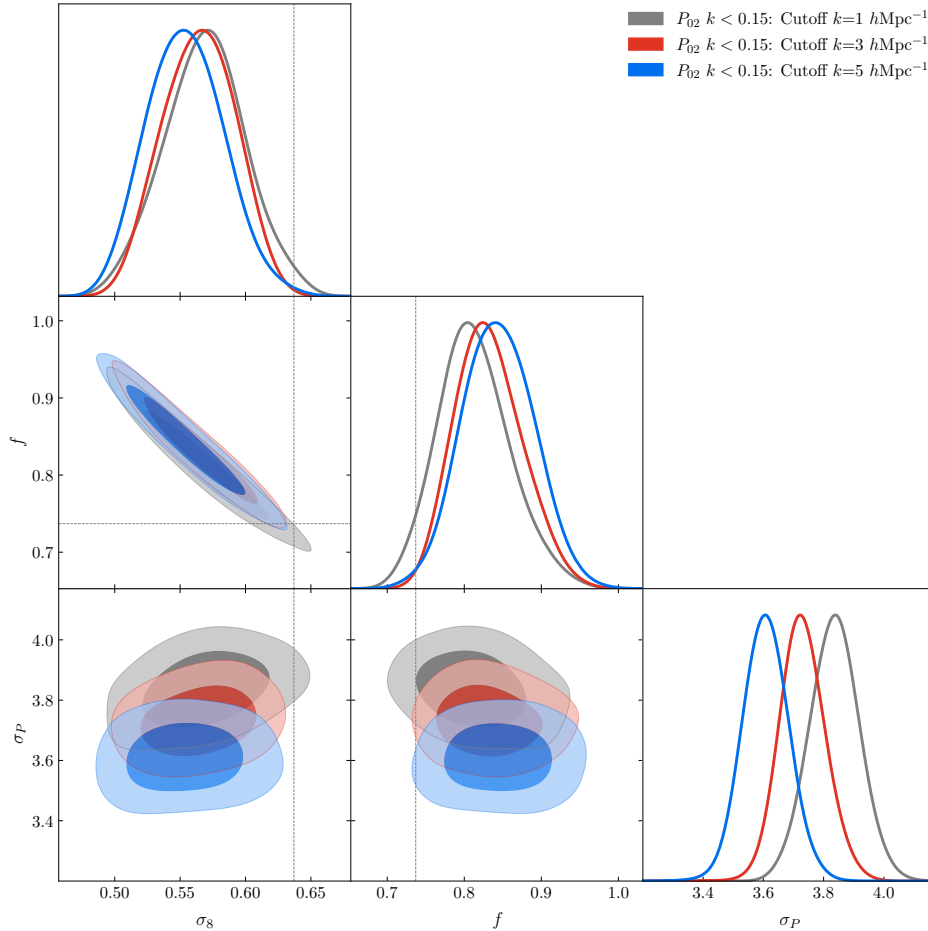


Figure 14. Posterior distributions of the recovered cosmological parameters σ_8 , f and the nuisance parameter σ_{FOG} , for the power spectrum data-vector in the NSERIES simulations as a function of the cutoff k . This cutoff k (not to be confused with the k_{max} of the data-vector, which we set to 0.15 in this plot), is the integral upper limit for the loop correction terms of the power spectrum model. We observe how the offset featured in Figure 7 is not ameliorated by a choice of a larger cutoff k ; rather, this choice is absorbed in the nuisance parameter σ_{P} , leaving the rest of the parameters largely unaffected.

References

- [1] L. Verde, A. F. Heavens, S. Matarrese, and L. Moscardini, “Large-scale bias in the Universe - II. Redshift-space bispectrum,” *Mon. Not. R. Astron. Soc.*, vol. 300, no. 3, pp. 747–756, 1998.
- [2] S. Matarrese, L. Verde, and A. F. Heavens, “Large-scale bias in the Universe: Bispectrum method,” *Mon. Not. R. Astron. Soc.*, vol. 290, no. 4, pp. 651–662, 1997.
- [3] E. Sefusatti, M. Crocce, S. Pueblas, and R. Scoccimarro, “Cosmology and the Bispectrum,” *Phys. Rev. D*, vol. 74, p. 023522, 2006.
- [4] J. N. Fry and E. Gaztanaga, “Biasing and hierarchical statistics in large-scale structure,” *The Astrophysical Journal*, vol. 413, pp. 447–452, 1993.
- [5] R. Ruggeri, E. Castorina, C. Carbone, and E. Sefusatti, “DEMNUi: massive neutrinos and the bispectrum of large scale structures,” *Journal of Cosmology and Astroparticle Physics*, vol. 2018, pp. 003–003, mar 2018.

- [6] C. Hahn, F. Villaescusa-Navarro, E. Castorina, and R. Scoccimarro, “Constraining $m\nu$ with the bispectrum. part i. breaking parameter degeneracies,” *Journal of Cosmology and Astroparticle Physics*, vol. 2020, pp. 040–040, mar 2020.
- [7] A. Oddo, F. Rizzo, E. Sefusatti, C. Porciani, and P. Monaco, “Cosmological parameters from the likelihood analysis of the galaxy power spectrum and bispectrum in real space,” *Journal of Cosmology and Astroparticle Physics*, vol. 2021, no. 11, p. 038, 2021.
- [8] N. Bartolo, E. Bellini, D. Bertacca, and S. Matarrese, “Matter bispectrum in cubic galileon cosmologies,” *Journal of Cosmology and Astroparticle Physics*, vol. 2013, no. 03, p. 034, 2013.
- [9] E. Bellini, R. Jimenez, and L. Verde, “Signatures of horndeski gravity on the dark matter bispectrum,” *Journal of Cosmology and Astroparticle Physics*, vol. 2015, no. 05, p. 057, 2015.
- [10] D. Bertacca, A. Raccanelli, N. Bartolo, M. Liguori, S. Matarrese, and L. Verde, “Relativistic wide-angle galaxy bispectrum on the light cone,” *Physical Review D*, vol. 97, no. 2, p. 023531, 2018.
- [11] H. Gil-Marín, F. Schmidt, W. Hu, R. Jimenez, and L. Verde, “The bispectrum of $f(r)$ cosmologies,” *Journal of Cosmology and Astroparticle Physics*, vol. 2011, pp. 019–019, nov 2011.
- [12] V. Yankelevich and C. Porciani, “Cosmological information in the redshift-space bispectrum,” *Monthly Notices of the Royal Astronomical Society*, vol. 483, no. 2, pp. 2078–2099, 2019.
- [13] W. R. Coulton, J. Liu, M. S. Madhavacheril, V. Böhm, and D. N. Spergel, “Constraining neutrino mass with the tomographic weak lensing bispectrum,” *Journal of Cosmology and Astroparticle Physics*, vol. 2019, no. 05, p. 043, 2019.
- [14] R. Ruggeri, E. Castorina, C. Carbone, and E. Sefusatti, “Demnuni: Massive neutrinos and the bispectrum of large scale structures,” *Journal of Cosmology and Astroparticle Physics*, vol. 2018, no. 03, p. 003, 2018.
- [15] P. Gagrani and L. Samushia, “Information content of the angular multipoles of redshift-space galaxy bispectrum,” *Monthly Notices of the Royal Astronomical Society*, vol. 467, no. 1, pp. 928–935, 2017.
- [16] D. Gualdi and L. Verde, “Galaxy redshift-space bispectrum: the Importance of Being Anisotropic,” *JCAP*, vol. 06, p. 041, 2020.
- [17] F. Rizzo, C. Moretti, K. Pardede, A. Eggemeier, A. Oddo, E. Sefusatti, C. Porciani, and P. Monaco, “The halo bispectrum multipoles in redshift space,” *Journal of Cosmology and Astroparticle Physics*, vol. 2023, no. 01, p. 031, 2023.
- [18] M. M. Ivanov, O. H. Philcox, G. Cabass, T. Nishimichi, M. Simonović, and M. Zaldarriaga, “Cosmology with the galaxy bispectrum multipoles: Optimal estimation and application to boss data,” *arXiv preprint arXiv:2302.04414*, 2023.
- [19] G. D’Amico, Y. Donath, M. Lewandowski, L. Senatore, and P. Zhang, “The one-loop bispectrum of galaxies in redshift space from the effective field theory of large-scale structure,” *arXiv preprint arXiv:2211.17130*, 2022.
- [20] T. Baldauf, U. Seljak, and L. Senatore, “Primordial non-gaussianity in the bispectrum of the halo density field,” *Journal of Cosmology and Astroparticle Physics*, vol. 2011, no. 04, p. 006, 2011.
- [21] A. M. Dizgah, M. Biagetti, E. Sefusatti, V. Desjacques, and J. Noreña, “Primordial non-gaussianity from biased tracers: likelihood analysis of real-space power spectrum and bispectrum,” *Journal of Cosmology and Astroparticle Physics*, vol. 2021, no. 05, p. 015, 2021.
- [22] D. Gualdi, S. Novell, H. Gil-Marín, and L. Verde, “Matter trispectrum: theoretical modelling and comparison to N-body simulations,” *Journal of Cosmology and Astroparticle Physics*, vol. 2021, pp. 015–015, Jan. 2021. arXiv: 2009.02290.

- [23] R. Scoccimarro, H. A. Feldman, J. N. Fry, and J. A. Frieman, “The Bispectrum of IRAS Redshift Catalogs,” *ApJ*, vol. 546, pp. 652–664, Jan. 2001.
- [24] L. Verde, A. F. Heavens, W. J. Percival, S. Matarrese, C. M. Baugh, J. Bland-Hawthorn, T. Bridges, R. Cannon, S. Cole, M. Colless, C. Collins, W. Couch, G. Dalton, R. De Propris, S. P. Driver, G. Efstathiou, R. S. Ellis, C. S. Frenk, K. Glazebrook, C. Jackson, O. Lahav, I. Lewis, S. Lumsden, S. Maddox, D. Madgwick, P. Norberg, J. A. Peacock, B. A. Peterson, W. Sutherland, and K. Taylor, “The 2dF Galaxy Redshift Survey: the bias of galaxies and the density of the Universe,” *MNRAS*, vol. 335, pp. 432–440, Sept. 2002.
- [25] H. Gil-Marín, W. J. Percival, L. Verde, J. R. Brownstein, C.-H. Chuang, F.-S. Kitaura, S. A. Rodríguez-Torres, and M. D. Olmstead, “The clustering of galaxies in the SDSS-III Baryon Oscillation Spectroscopic Survey: RSD measurement from the power spectrum and bispectrum of the DR12 BOSS galaxies,” *Mon. Not. Roy. Astron. Soc.*, vol. 465, no. 2, pp. 1757–1788, 2017.
- [26] B. Reid, S. Ho, N. Padmanabhan, W. J. Percival, J. Tinker, R. Tojeiro, M. White, D. J. Eisenstein, C. Maraston, A. J. Ross, A. G. Sánchez, D. Schlegel, E. Sheldon, M. A. Strauss, D. Thomas, D. Wake, F. Beutler, D. Bizyaev, A. S. Bolton, J. R. Brownstein, C.-H. Chuang, K. Dawson, P. Harding, F.-S. Kitaura, A. Leauthaud, K. Masters, C. K. McBride, S. More, M. D. Olmstead, D. Oravetz, S. E. Nuza, K. Pan, J. Parejko, J. Pforr, F. Prada, S. Rodríguez-Torres, S. Salazar-Albornoz, L. Samushia, D. P. Schneider, C. G. Scóccola, A. Simmons, and M. Vargas-Magana, “SDSS-III Baryon Oscillation Spectroscopic Survey Data Release 12: galaxy target selection and large-scale structure catalogues,” *MNRAS*, vol. 455, pp. 1553–1573, Jan. 2016.
- [27] A. J. Ross, J. Bautista, R. Tojeiro, S. Alam, S. Bailey, E. Burtin, J. Comparat, K. S. Dawson, A. de Mattia, H. du Mas des Bourboux, H. Gil-Marín, J. Hou, H. Kong, B. W. Lyke, F. G. Mohammad, J. Moustakas, E.-M. Mueller, A. D. Myers, W. J. Percival, A. Raichoor, M. Rezaie, H.-J. Seo, A. Smith, J. L. Tinker, P. Zarrouk, C. Zhao, G.-B. Zhao, D. Bizyaev, J. Brinkmann, J. R. Brownstein, A. C. Rosell, S. Chabanier, P. D. Choi, C.-H. Chuang, I. Cruz-Gonzalez, A. de la Macorra, S. de la Torre, S. Escoffier, S. Fromenteau, A. Higley, E. Jullo, J.-P. Kneib, J. N. McLane, A. Muñoz-Gutiérrez, R. Neveux, J. A. Newman, C. Nitschelm, N. Palanque-Delabrouille, R. Paviot, A. R. Pullen, G. Rossi, V. Ruhlmann-Kleider, D. P. Schneider, M. V. Magaña, M. Vivek, and Y. Zhang, “The Completed SDSS-IV extended Baryon Oscillation Spectroscopic Survey: Large-scale structure catalogues for cosmological analysis,” *MNRAS*, vol. 498, pp. 2354–2371, Oct. 2020.
- [28] A. Raichoor, A. de Mattia, A. J. Ross, C. Zhao, S. Alam, S. Avila, J. Bautista, J. Brinkmann, J. R. Brownstein, E. Burtin, M. J. Chapman, C.-H. Chuang, J. Comparat, K. S. Dawson, A. Dey, H. du Mas des Bourboux, J. Elvin-Poole, V. Gonzalez-Perez, C. Gorgoni, J.-P. Kneib, H. Kong, D. Lang, J. Moustakas, A. D. Myers, E.-M. Müller, S. Nadathur, J. A. Newman, W. J. Percival, M. Rezaie, G. Rossi, V. Ruhlmann-Kleider, D. J. Schlegel, D. P. Schneider, H.-J. Seo, A. Tamone, J. L. Tinker, R. Tojeiro, M. Vivek, C. Yèche, and G.-B. Zhao, “The completed SDSS-IV extended Baryon Oscillation Spectroscopic Survey: large-scale structure catalogues and measurement of the isotropic BAO between redshift 0.6 and 1.1 for the Emission Line Galaxy Sample,” *MNRAS*, vol. 500, pp. 3254–3274, Jan. 2021.
- [29] M. Levi, C. Bebek, T. Beers, R. Blum, R. Cahn, D. Eisenstein, B. Flaugher, K. Honscheid, R. Kron, O. Lahav, P. McDonald, N. Roe, D. Schlegel, and representing the DESI collaboration, “The DESI Experiment, a whitepaper for Snowmass 2013,” *ArXiv e-prints*, Aug. 2013.
- [30] R. Laureijs *et al.*, “Euclid Definition Study Report,” 2011.
- [31] P. A. Abell *et al.*, “LSST Science Book, Version 2.0,” 2009.
- [32] J. Green *et al.*, “Wide-Field InfraRed Survey Telescope (WFIRST) Final Report,” 8 2012.
- [33] F. Villaescusa-Navarro, C. Hahn, E. Massara, A. Banerjee, A. M. Delgado, D. K. Ramanah,

- T. Charnock, E. Giusarma, Y. Li, E. Allys, A. Brochard, C.-T. Chiang, S. He, A. Pisani, A. Obuljen, Y. Feng, E. Castorina, G. Contardo, C. D. Kreisch, A. Nicola, R. Scoccimarro, L. Verde, M. Viel, S. Ho, S. Mallat, B. Wandelt, and D. N. Spergel, “The Quijote simulations,” *The Astrophysical Journal Supplement Series*, vol. 250, p. 2, Aug. 2020. arXiv: 1909.05273.
- [34] R. E. Angulo, S. Foreman, M. Schmittfull, and L. Senatore, “The one-loop matter bispectrum in the effective field theory of large scale structures,” *Journal of Cosmology and Astroparticle Physics*, vol. 2015, no. 10, p. 039, 2015.
- [35] M. M. Ivanov, O. H. Philcox, T. Nishimichi, M. Simonović, M. Takada, and M. Zaldarriaga, “Precision analysis of the redshift-space galaxy bispectrum,” *Physical Review D*, vol. 105, no. 6, p. 063512, 2022.
- [36] R. Scoccimarro and H. M. Couchman, “A fitting formula for the non-linear evolution of the bispectrum,” *Monthly Notices of the Royal Astronomical Society*, vol. 325, pp. 1312–1316, 2001.
- [37] H. Gil-Marín, C. Wagner, F. Fragkoudi, R. Jimenez, and L. Verde, “An improved fitting formula for the dark matter bispectrum,” *JCAP*, vol. 02, p. 047, 2012.
- [38] H. Gil-Marín, C. Wagner, J. Noreña, L. Verde, and W. Percival, “Dark matter and halo bispectrum in redshift space: theory and applications,” *JCAP*, vol. 12, p. 029, 2014.
- [39] J. Lesgourgues, “The Cosmic Linear Anisotropy Solving System (CLASS) I: Overview,” 4 2011.
- [40] F. Bernardeau, S. Colombi, E. Gaztañaga, and R. Scoccimarro, “Large-scale structure of the Universe and cosmological perturbation theory,” *Phys. Rep.*, vol. 367, pp. 1–248, Sept. 2002.
- [41] M. Crocce and R. Scoccimarro, “Renormalized cosmological perturbation theory,” *Physical Review D*, vol. 73, mar 2006.
- [42] H. Gil-Marín, C. Wagner, L. Verde, C. Porciani, and R. Jimenez, “Perturbation theory approach for the power spectrum: from dark matter in real space to massive haloes in redshift space,” *Journal of Cosmology and Astroparticle Physics*, vol. 2012, pp. 029–029, nov 2012.
- [43] J. Fry, “The galaxy correlation hierarchy in perturbation theory,” *The Astronomical Journal*, vol. 53, pp. 499–510, 1983.
- [44] A. Taruya, T. Nishimichi, and S. Saito, “Baryon acoustic oscillations in 2d: Modeling redshift-space power spectrum from perturbation theory,” *Physical Review D*, vol. 82, sep 2010.
- [45] T. Nishimichi and A. Taruya, “Baryon acoustic oscillations in 2d. II. redshift-space halo clustering in n-body simulations,” *Physical Review D*, vol. 84, aug 2011.
- [46] F. Beutler, S. Saito, H.-J. Seo, J. Brinkmann, K. S. Dawson, D. J. Eisenstein, A. Font-Ribera, S. Ho, C. K. McBride, F. Montesano, *et al.*, “The clustering of galaxies in the sdss-iii baryon oscillation spectroscopic survey: testing gravity with redshift space distortions using the power spectrum multipoles,” *Monthly Notices of the Royal Astronomical Society*, vol. 443, no. 2, pp. 1065–1089, 2014.
- [47] T. Baldauf, U. Seljak, V. Desjacques, and P. McDonald, “Evidence for quadratic tidal tensor bias from the halo bispectrum,” *Physical Review D*, vol. 86, no. 8, p. 083540, 2012.
- [48] S. Saito, T. Baldauf, Z. Vlah, U. Seljak, T. Okumura, and P. McDonald, “Understanding higher-order nonlocal halo bias at large scales by combining the power spectrum with the bispectrum,” *Physical Review D*, vol. 90, no. 12, p. 123522, 2014.
- [49] S. Brieden, H. Gil-Marín, and L. Verde, “PT challenge: validation of ShapeFit on large-volume, high-resolution mocks,” *J. Cosmology Astropart. Phys.*, vol. 2022, p. 005, June 2022.
- [50] J. C. Jackson, “A critique of rees's theory of primordial gravitational radiation,” *Monthly Notices of the Royal Astronomical Society*, vol. 156, pp. 1P–5P, feb 1972.
- [51] R. Scoccimarro, H. M. P. Couchman, and J. A. Frieman, “The Bispectrum as a Signature of Gravitational Instability in Redshift-Space,” *Astrophys. J.*, vol. 517, pp. 531–540, 1999.

- [52] C. Alcock and B. Paczynski, “An evolution free test for non-zero cosmological constant,” *Nature*, vol. 281, pp. 358–359, 1979.
- [53] W. Ballinger, J. Peacock, and A. Heavens, “Measuring the cosmological constant with redshift surveys,” *Monthly Notices of the Royal Astronomical Society*, vol. 282, no. 3, pp. 877–888, 1996.
- [54] H. Gil-Marín, W. J. Percival, L. Verde, J. R. Brownstein, C.-H. Chuang, F.-S. Kitaura, S. A. Rodríguez-Torres, and M. D. Olmstead, “The clustering of galaxies in the SDSS-III Baryon Oscillation Spectroscopic Survey: RSD measurement from the power spectrum and bispectrum of the DR12 BOSS galaxies,” *Monthly Notices of the Royal Astronomical Society*, vol. 465, pp. 1757–1788, Feb. 2017.
- [55] A. Hamilton, “Measuring omega and the real correlation function from the redshift correlation function,” *The Astrophysical Journal*, vol. 385, pp. L5–L8, 1992.
- [56] S. Cole, K. B. Fisher, and D. H. Weinberg, “Fourier analysis of redshift-space distortions and the determination of ω ,” *Monthly Notices of the Royal Astronomical Society*, vol. 267, no. 3, pp. 785–799, 1994.
- [57] N. S. Sugiyama, S. Saito, F. Beutler, and H.-J. Seo, “A complete fft-based decomposition formalism for the redshift-space bispectrum,” *Monthly Notices of the Royal Astronomical Society*, vol. 484, no. 1, pp. 364–384, 2019.
- [58] E. Sefusatti, “1-loop Perturbative Corrections to the Matter and Galaxy Bispectrum with non-Gaussian Initial Conditions,” *Phys. Rev. D*, vol. 80, p. 123002, 2009.
- [59] O. H. Philcox, M. M. Ivanov, G. Cabass, M. Simonović, M. Zaldarriaga, and T. Nishimichi, “Cosmology with the redshift-space galaxy bispectrum monopole at one-loop order,” *Physical Review D*, vol. 106, no. 4, p. 043530, 2022.
- [60] A. Eggemeier, R. Scoccimarro, R. E. Smith, M. Crocce, A. Pezzotta, and A. G. Sánchez, “Testing one-loop galaxy bias: Joint analysis of power spectrum and bispectrum,” *Physical Review D*, vol. 103, no. 12, p. 123550, 2021.
- [61] D. Gualdi, H. Gil-Marín, M. Manera, B. Joachimi, and O. Lahav, “Geometrical compression: a new method to enhance the BOSS galaxy bispectrum monopole constraints,” *Monthly Notices of the Royal Astronomical Society: Letters*, vol. 484, pp. L29–L34, Mar. 2019. arXiv: 1901.00987.
- [62] D. Gualdi, H. Gil-Marín, M. Manera, B. Joachimi, and O. Lahav, “Geomax: beyond linear compression for three-point galaxy clustering statistics,” *Monthly Notices of the Royal Astronomical Society*, vol. 497, no. 1, pp. 776–792, 2020.
- [63] R. Scoccimarro, S. Colombi, J. N. Fry, J. A. Frieman, E. Hivon, and A. Melott, “Nonlinear evolution of the bispectrum of cosmological perturbations,” *The Astrophysical Journal*, vol. 496, no. 2, p. 586, 1998.
- [64] R. E. Smith, R. K. Sheth, and R. Scoccimarro, “Analytic model for the bispectrum of galaxies in redshift space,” *Physical Review D*, vol. 78, no. 2, p. 023523, 2008.
- [65] R. E. Smith, J. A. Peacock, A. Jenkins, S. White, C. Frenk, F. Pearce, P. A. Thomas, G. Efstathiou, and H. Couchman, “Stable clustering, the halo model and non-linear cosmological power spectra,” *Monthly Notices of the Royal Astronomical Society*, vol. 341, no. 4, pp. 1311–1332, 2003.
- [66] R. Takahashi, M. Sato, T. Nishimichi, A. Taruya, and M. Oguri, “Revising the halofit model for the nonlinear matter power spectrum,” *The Astrophysical Journal*, vol. 761, no. 2, p. 152, 2012.
- [67] D. Gualdi, H. Gil-Marín, and L. Verde, “Joint analysis of anisotropic power spectrum, bispectrum and trispectrum: application to N-body simulations,” *arXiv:2104.03976 [astro-ph]*, Apr. 2021. arXiv: 2104.03976.

- [68] R. Scoccimarro, “Transients from initial conditions: a perturbative analysis,” *Monthly Notices of the Royal Astronomical Society*, vol. 299, no. 4, pp. 1097–1118, 1998.
- [69] M. Crocce, S. Pueblas, and R. Scoccimarro, “Transients from initial conditions in cosmological simulations,” *Monthly Notices of the Royal Astronomical Society*, vol. 373, no. 1, pp. 369–381, 2006.
- [70] M. Michaux, O. Hahn, C. Rampf, and R. E. Angulo, “Accurate initial conditions for cosmological n-body simulations: Minimizing truncation and discreteness errors,” *Monthly Notices of the Royal Astronomical Society*, vol. 500, no. 1, pp. 663–683, 2021.
- [71] P. Collaboration, N. Aghanim, Y. Akrami, M. Ashdown, J. Aumont, C. Baccigalupi, M. Ballardini, A. J. Banday, R. B. Barreiro, N. Bartolo, S. Basak, R. Battye, K. Benabed, J. P. Bernard, M. Bersanelli, P. Bielewicz, J. J. Bock, J. R. Bond, J. Borrill, F. R. Bouchet, F. Boulanger, M. Bucher, C. Burigana, R. C. Butler, E. Calabrese, J. F. Cardoso, J. Carron, A. Challinor, H. C. Chiang, J. Chluba, L. P. L. Colombo, C. Combet, D. Contreras, B. P. Crill, F. Cuttaia, P. de Bernardis, G. de Zotti, J. Delabrouille, J. M. Delouis, E. D. Valentino, J. M. Diego, O. Doré, M. Douspis, A. Ducout, X. Dupac, S. Dusini, G. Efstathiou, F. Elsner, T. A. Enßlin, H. K. Eriksen, Y. Fantaye, M. Farhang, J. Fergusson, R. Fernandez-Cobos, F. Finelli, F. Forastieri, M. Frailis, A. A. Fraisse, E. Franceschi, A. Frolov, S. Galeotta, S. Galli, K. Ganga, R. T. Génova-Santos, M. Gerbino, T. Ghosh, J. González-Nuevo, K. M. Górski, S. Gratton, A. Gruppuso, J. E. Gudmundsson, J. Hamann, W. Handley, F. K. Hansen, D. Herranz, S. R. Hildebrandt, E. Hivon, Z. Huang, A. H. Jaffe, W. C. Jones, A. Karakci, E. Keihänen, R. Keskitalo, K. Kiiveri, J. Kim, T. S. Kisner, L. Knox, N. Krachmalnicoff, M. Kunz, H. Kurki-Suonio, G. Lagache, J. M. Lamarre, A. Lasenby, M. Lattanzi, C. R. Lawrence, M. L. Jeune, P. Lemos, J. Lesgourgues, F. Levrier, A. Lewis, M. Liguori, P. B. Lilje, M. Lilley, V. Lindholm, M. López-Cañiego, P. M. Lubin, Y. Z. Ma, J. F. Macías-Pérez, G. Maggio, D. Maino, N. Mandolesi, A. Mangilli, A. Marcos-Caballero, M. Maris, P. G. Martin, M. Martinelli, E. Martínez-González, S. Matarrese, N. Mauri, J. D. McEwen, P. R. Meinhold, A. Melchiorri, A. Mennella, M. Migliaccio, M. Millea, S. Mitra, M. A. Miville-Deschênes, D. Molinari, L. Montier, G. Morgante, A. Moss, P. Natoli, H. U. Nørgaard-Nielsen, L. Pagano, D. Paoletti, B. Partridge, G. Patanchon, H. V. Peiris, F. Perrotta, V. Pettorino, F. Piacentini, L. Polastri, G. Polenta, J. L. Puget, J. P. Rachen, M. Reinecke, M. Remazeilles, A. Renzi, G. Rocha, C. Rosset, G. Roudier, J. A. Rubiño-Martín, B. Ruiz-Granados, L. Salvati, M. Sandri, M. Savelainen, D. Scott, E. P. S. Shellard, C. Sirignano, G. Sirri, L. D. Spencer, R. Sunyaev, A. S. Suur-Uski, J. A. Tauber, D. Tavagnacco, M. Tenti, L. Toffolatti, M. Tomasi, T. Trombetti, L. Valenziano, J. Valiviita, B. V. Tent, L. Vibert, P. Vielva, F. Villa, N. Vittorio, B. D. Wandelt, I. K. Wehus, M. White, S. D. M. White, A. Zacchei, and A. Zonca, “Planck 2018 results. vi. cosmological parameters,” 2018.
- [72] S. Satpathy, S. Alam, S. Ho, M. White, N. A. Bahcall, F. Beutler, J. R. Brownstein, C.-H. Chuang, D. J. Eisenstein, J. N. Grieb, *et al.*, “The clustering of galaxies in the completed sdss-iii baryon oscillation spectroscopic survey: On the measurement of growth rate using galaxy correlation functions,” *Monthly Notices of the Royal Astronomical Society*, vol. 469, no. 2, pp. 1369–1382, 2017.
- [73] S. Alam, M. Ata, S. Bailey, F. Beutler, D. Bizyaev, J. A. Blazek, A. S. Bolton, J. R. Brownstein, A. Burden, C.-H. Chuang, *et al.*, “The clustering of galaxies in the completed sdss-iii baryon oscillation spectroscopic survey: cosmological analysis of the dr12 galaxy sample,” *Monthly Notices of the Royal Astronomical Society*, vol. 470, no. 3, pp. 2617–2652, 2017.
- [74] C. Hahn, R. Scoccimarro, M. R. Blanton, J. L. Tinker, and S. A. Rodríguez-Torres, “The effect of fibre collisions on the galaxy power spectrum multipoles,” *Monthly Notices of the Royal Astronomical Society*, vol. 467, no. 2, pp. 1940–1956, 2017.
- [75] G. Hinshaw, D. Larson, E. Komatsu, D. N. Spergel, C. Bennett, J. Dunkley, M. Nolta,

- M. Halpern, R. Hill, N. Odegard, *et al.*, “Nine-year wilkinson microwave anisotropy probe (wmap) observations: cosmological parameter results,” *The Astrophysical Journal Supplement Series*, vol. 208, no. 2, p. 19, 2013.
- [76] M. Tegmark, “Measuring cosmological parameters with galaxy surveys,” *Physical Review Letters*, vol. 79, no. 20, p. 3806, 1997.
- [77] F.-S. Kitaura, S. Rodriguez-Torres, C.-H. Chuang, C. Zhao, F. Prada, H. Gil-Marín, H. Guo, G. Yepes, A. Klypin, C. G. Scóccola, *et al.*, “The clustering of galaxies in the sdss-iii baryon oscillation spectroscopic survey: mock galaxy catalogues for the boss final data release,” *Monthly Notices of the Royal Astronomical Society*, vol. 456, no. 4, pp. 4156–4173, 2016.
- [78] R. de Putter, C. Wagner, O. Mena, L. Verde, and W. J. Percival, “Thinking outside the box: effects of modes larger than the survey on matter power spectrum covariance,” *J. Cosmology Astropart. Phys.*, vol. 2012, p. 019, Apr. 2012.
- [79] G. D’Amico, Y. Donath, M. Lewandowski, L. Senatore, and P. Zhang, “The boss bispectrum analysis at one loop from the effective field theory of large-scale structure,” *arXiv preprint arXiv:2206.08327*, 2022.
- [80] E. Sefusatti, M. Crocce, and V. Desjacques, “The matter bispectrum in N-body simulations with non-Gaussian initial conditions,” *MNRAS*, vol. 406, pp. 1014–1028, Aug. 2010.
- [81] A. Oddo, E. Sefusatti, C. Porciani, P. Monaco, and A. G. Sánchez, “Toward a robust inference method for the galaxy bispectrum: likelihood function and model selection,” *Journal of Cosmology and Astroparticle Physics*, vol. 2020, pp. 056–056, mar 2020.
- [82] S. Brieden, H. Gil-Marín, and L. Verde, “Shapefit: extracting the power spectrum shape information in galaxy surveys beyond bao and rsd,” *Journal of Cosmology and Astroparticle Physics*, vol. 2021, no. 12, p. 054, 2021.
- [83] D. Foreman-Mackey, D. W. Hogg, D. Lang, and J. Goodman, “emcee: The MCMC hammer,” *Publications of the Astronomical Society of the Pacific*, vol. 125, pp. 306–312, mar 2013.
- [84] E. Sellentin and A. F. Heavens, “Parameter inference with estimated covariance matrices,” *Mon. Not. Roy. Astron. Soc.*, vol. 456, no. 1, pp. L132–L136, 2016.
- [85] K. C. Chan and L. Blot, “Assessment of the information content of the power spectrum and bispectrum,” *Physical Review D*, vol. 96, no. 2, p. 023528, 2017.
- [86] M. Sato and T. Nishimichi, “Impact of the non-gaussian covariance of the weak lensing power spectrum and bispectrum on cosmological parameter estimation,” *Physical Review D*, vol. 87, no. 12, p. 123538, 2013.
- [87] M. Colavincenzo, E. Sefusatti, P. Monaco, L. Blot, M. Crocce, M. Lippich, A. G. Sánchez, M. A. Alvarez, A. Agrawal, S. Avila, *et al.*, “Comparing approximate methods for mock catalogues and covariance matrices—iii: bispectrum,” *Monthly Notices of the Royal Astronomical Society*, vol. 482, no. 4, pp. 4883–4905, 2019.
- [88] M. Biagetti, L. Castiblanco, J. Noreña, and E. Sefusatti, “The covariance of squeezed bispectrum configurations,” *Journal of Cosmology and Astroparticle Physics*, vol. 2022, no. 09, p. 009, 2022.
- [89] H. Gil-Marín, J. E. Bautista, R. Paviot, M. Vargas-Magaña, S. de la Torre, S. Fromenteau, S. Alam, S. Ávila, E. Burtin, C.-H. Chuang, K. S. Dawson, J. Hou, A. de Mattia, F. G. Mohammad, E.-M. Müller, S. Nadathur, R. Neveux, W. J. Percival, A. Raichoor, M. Rezaie, A. J. Ross, G. Rossi, V. Ruhlmann-Kleider, A. Smith, A. Tamone, J. L. Tinker, R. Tojeiro, Y. Wang, G.-B. Zhao, C. Zhao, J. Brinkmann, J. R. Brownstein, P. D. Choi, S. Escoffier, A. de la Macorra, J. Moon, J. A. Newman, D. P. Schneider, H.-J. Seo, and M. Vivek, “The Completed SDSS-IV extended Baryon Oscillation Spectroscopic Survey: measurement of the BAO and growth rate of structure of the luminous red galaxy sample from the anisotropic power spectrum between redshifts 0.6 and 1.0,” *MNRAS*, vol. 498, pp. 2492–2531, Oct. 2020.

- [90] M. Maus, S.-F. Chen, and M. White, “A comparison of template vs. direct model fitting for redshift-space distortions in boss,” *arXiv preprint arXiv:2302.07430*, 2023.
- [91] M. Maus *et al.*, “In prep.,” 2023.
- [92] Y. Lai *et al.*, “In prep.,” 2023.
- [93] K. Pardede, F. Rizzo, M. Biagetti, E. Castorina, E. Sefusatti, and P. Monaco, “Bispectrum-window convolution via hankel transform,” *Journal of Cosmology and Astroparticle Physics*, vol. 2022, no. 10, p. 066, 2022.
- [94] D. Alkhanishvili, C. Porciani, and E. Sefusatti, “Window function convolution with deep neural network models,” *Astronomy & Astrophysics*, vol. 669, p. L2, 2023.